

This work was written as part of one of the author's official duties as an Employee of the United States Government and is therefore a work of the United States Government. In accordance with 17 U.S.C. 105, no copyright protection is available for such works under U.S. Law.

Public Domain Mark 1.0

<https://creativecommons.org/publicdomain/mark/1.0/>

Access to this work was provided by the University of Maryland, Baltimore County (UMBC) ScholarWorks@UMBC digital repository on the Maryland Shared Open Access (MD-SOAR) platform.

Please provide feedback

Please support the ScholarWorks@UMBC repository by emailing scholarworks-group@umbc.edu and telling us what having access to this work means to you and why it's important to you. Thank you.



Revised and extended benchmark results for Rayleigh scattering of sunlight in spherical atmospheres

Sergey Korkin^{a,*}, Eun-Su Yang^b, Robert Spurr^c, Claudia Emde^d, Nikolay Krotkov^e, Alexander Vasilkov^b, David Haffner^b, Jungbin Mok^f, Alexei Lyapustin^e

^a Universities Space Research Association GESTAR, Columbia, MD, USA

^b Science Systems and Applications Inc., Lanham, MD, USA

^c RT Solutions Inc., Cambridge, MA, USA

^d Meteorological Institute, Ludwig-Maximilians-University, Germany

^e NASA Goddard Space Flight Center, Greenbelt, MD, USA

^f University of Maryland ESSIC, College Park, MD, USA

ARTICLE INFO

Article history:

Received 13 May 2020

Revised 15 June 2020

Accepted 18 June 2020

Available online 20 June 2020

ABSTRACT

While most of traditional Earth-atmosphere satellite remote sensing relies on radiative transfer (RT) in the plane parallel geometry, effects of sphericity are important at high sun and view zenith angles. Broad understanding of these effects is limited and, contrary to the plane-parallel case, finding accurate numerical results to test spherical RT codes is not easy. This paper aims to partially fill in this gap. Using the full-spherical RT code MYSTIC (Monte Carlo), and the plane-parallel RT code VLIDORT (discrete ordinates) corrected for atmospheric sphericity in the single and multiple scattering, we reproduced with better accuracy and extended the benchmark results by Adams & Kattawar [1].

© 2020 Elsevier Ltd. All rights reserved.

1. Introduction

Radiative Transfer (RT) codes are key components in the satellite remote sensing retrieval algorithms (e.g., [20,53,78]). In general, an RT model is a suite of scientific software for the numerical simulation of light scattering in the Earth's atmosphere-surface environment. The testing of any RT code against reliable (accurate and reproducible) benchmarks is an essential step in software development and lifetime maintenance. Benchmark data must be reported numerically with sufficient accuracy. This paper deals with benchmark results for RT codes that simulate multiple scattering of monochromatic solar light over black surface in a spherical atmosphere of the Earth. We deal only with Rayleigh scattering in the absence of any trace gas absorption, and we ignore the effects of polarization and solar rays bending due to atmospheric refraction.

In many retrieval applications, RT modeling has been done using a plane-parallel model [49,86]; this is feasible because the Earth radius, ~6370 km, is much larger than a typical height for low Earth orbit (LEO) satellite platforms, for example ~700 km for the NASA A-Train constellation. The plane-parallel approximation is usually assumed to be valid for the solar (SZA) and/or view (VZA) zenith angles not exceeding 75° ([58]: p.105, Sec. 2.5.4 “Equivalent

Paths: Spherical Earth”; [50]: p.235, Sec.15.2.3.1 “Ground-based measurements”), although the level of accuracy is unclear from these references. However, modern Earth observation systems often go beyond these constraints, including the EPIC instrument on the Deep Space Climate Observatory (DSCOVR) platform located at the Sun-Earth Lagrange L-1 point at 1.5M km orbit, operational meteorological geostationary satellites (at ~36K km orbit) including GOES-R, HIMAWARI, KOMPSAT and others. The consideration of Earth sphericity is important even for the low Earth orbit observations, e.g., from MODIS and VIIRS near Polar regions where the SZA is high, for the limb observations, e.g. from SCIAMACHY and OMPS Limb Profiler, as well as for the ground-based atmospheric remote sensing during early morning and late evening hours [38,88]. In these situations, the differences in optical paths and the solar-view geometries between spherical and plane-parallel atmospheres can no longer be ignored (Fig. 1). To remain accurate in these cases, RT codes must account for the curvature of the Earth's atmosphere (hereafter, *sphericity*, - hence “spherical model” as opposed to “plane-parallel model”).

In addition to changes in the optical path, the zenith angles take different values at the top (TOA) and bottom (BOA) of atmosphere (Fig. 2). For the MODIS maximum scan angle of 55°,

* Corresponding author.

E-mail address: sergey.v.korkin@nasa.gov (S. Korkin).

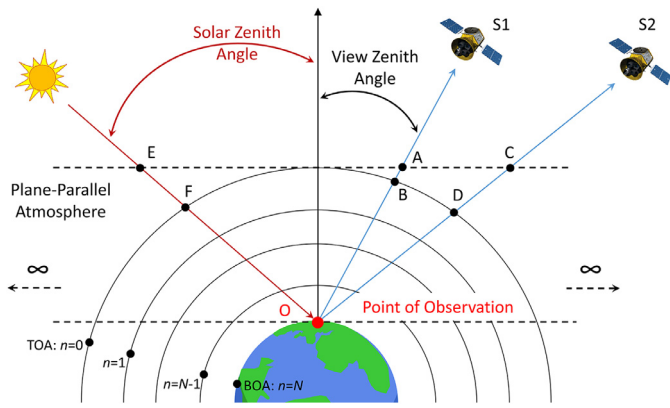


Fig. 1. The difference in the optical path between plane-parallel (dashed line) and spherical (solid line) atmospheres increases with larger VZA (segment AB for satellite position S1 and segment CD for position S2). The same effect applies to the solar beam (segment EF).

$VZA_{TOA} = 63^\circ$ and $VZA_{BOA} = 65^\circ$, which follows from

$$\sin \theta_{BOA} = \left(1 + \frac{h}{R_E}\right) \sin \theta_{TOA}. \quad (1)$$

The right panel in Fig. 2 shows the VZA to the scan angle ratio at TOA and BOA according to Eq. (1). For a plane-parallel atmosphere, all VZAs would be 55° for the MODIS maximum scan angle.

In Eq. (1) and in the sequel, θ stands for the VZA, $R_E = 6371$ (km) is the mean Earth radius, and h (km) is an arbitrary height above the ground. Eq. (1) shows that $\theta_{BOA} \geq \theta_{TOA}$. At some critical angle VZA_{TOA} given by

$$\theta_{TOA}^{Critical} = \sin^{-1} \left(\frac{R_E}{R_E + h} \right), \quad (2)$$

the line-of-sight (LOS) hits the ground at 90° . For any value of VZA_{TOA} exceeding this critical angle, the line of sight goes horizontally through a tangent height in the atmosphere, something which is not possible in a plane-parallel medium. When the Earth is observed from a height $h = 100$ km, the critical angle is $\theta_{TOA}^{Critical} \approx 79.9^\circ$.

The exigencies of spherical geometry lead to the violation of several fundamental results in RT theory which are valid for plane-parallel media. For example, the principle of reciprocity

$$\mu I(\mu, \mu_0, \varphi) = \mu_0 I(\mu_0, \mu, \varphi), \quad (3)$$

where I is the intensity, μ , μ_0 , and φ are the cosines of VZA, SZA, and azimuth, respectively, is no longer valid in a spherical medium. Adams & Kattawar, [1]: p.151, note that for single scattering alone, the right hand side of Eq. (3) is up to 3 times higher than the left for Rayleigh scattering. Another example that is not valid for spherical media is the natural azimuth independence of the intensity for isotropically scattering plane-parallel atmospheres. In a spherical atmosphere, the scattered intensity always depends on the relative azimuth, except for the overhead sun configuration. The azimuthal asymmetry comes from the dependence of the direct solar beam attenuation factor on relative azimuth, [35]: p.380.

The plane-parallel atmosphere is, by definition, horizontally infinite. It cannot deal with twilight, refraction, and the existence of the day/night line (terminator). These fundamental issues make it difficult to find a simple yet general sphericity correction factor, which can be applied to a plane-parallel RT model in order to generate radiation fields that are sufficiently close to spherical RT equivalents, in a wide range of applications. In this paper, we turn our attention to two RT codes that can simulate, precisely or approximately, multiple scattering of light in a spherical atmosphere.

We leave aside detailed performance considerations (accuracy and runtime) of full-spherical and approximate plane-parallel RT codes, as well as the combining single and/or double scattering in spherical geometry with higher-order scattering from the plane-parallel RT model.

RT codes require validation against reliable numerical data published in the open literature. A complete literature review is almost impossible. However, our analysis of about 90 references published from the 1960's to the present day shows that there is a lack of accurate (numbers, not figures), reliable (easy to reproduce, with known accuracy), and general (different solar-view geometries and atmosphere-surface properties) benchmark results for spherical geometry. This paper aims to partially fill the gap by: 1) reproducing, with better accuracy, the existing benchmark results generated by Adams & Kattawar, [1]: p.143, Table 1, these being the most closely related to modern requirements for satellite remote sensing applications, and 2) extending their results beyond the principal plane using two state-of-the-art RT codes, a true-spherical Monte Carlo code MYSTIC from the libRadtran¹ package [27,56,57] and the discrete ordinate VLIDORT code [84] corrected for atmospheric sphericity. Both codes have been in existence for some time and are widely used in the remote sensing community. In this paper, we refer to the work by Adams & Kattawar [1] as A & K.

The paper is structured as follows. First, in the "References overview", we highlight the need for publication of accurate benchmark results to test spherical RT codes. In the next section on "Methodology", we briefly describe the spherical RT implementation in MYSTIC (which is the baseline code in our research), and the discrete-ordinate treatment in VLIDORT. In the following section, we discuss the accuracy of the existing and new benchmarks ("Numerical results and discussion"). Aspects of spherical geometry as applied to RT are discussed in the Appendices. We conclude the paper with a Summary.

2. References overview

Nowadays, the theory of light scattering in a spherical atmosphere has been well developed. Numerous papers contain mathematical formalisms, e.g. Lenoble [48], Bellman [4], Smokty [79], to name just a few of the earliest. Rozenberg, [76]: p.125, Chapter III "Principles of the twilight theory", describes in detail the computation of optical paths in a spherical atmosphere but does not treat multiple scattering of light. The entire monograph by Sen & Wilson [77] deals with RT in curved media, including Chapter VII "Numerical methods for transfer problems in spherical geometry" (p.321), which, despite that name, has no reported numerical results. Sobolev, [80]: p.213, Chapter 11 "Spherical atmospheres", calculates the brightness of a planet close to the terminator for the isotropic scattering case (p.229: Table 11.2), using an approximate numerical solution. His results agree qualitatively with observations of Venus, but the numerical accuracy is unclear. In Chapter 4 "Monte Carlo methods for solving direct and inverse problems of the theory of radiative transfer in a spherical atmosphere" of Marchuk [54], there are extensive numerical results compared against measurements. In that work, realistic atmospheric models (gas absorption profiles, aerosol, surface reflectance, 14 wavelengths, etc.) were assumed. These "too realistic" scenarios are hard to reproduce with confidence. Also, the authors report ~10% simulation error (p.104), which is not acceptable for our goals in this paper. However, throughout the chapter, Marchuk and co-authors do present numbers for intensities as a function of the atmospheric and surface optical properties, location of the observer in the atmosphere, the role of polarization, and for sin-

¹ www.libradtran.org (accessed June 12, 2020)

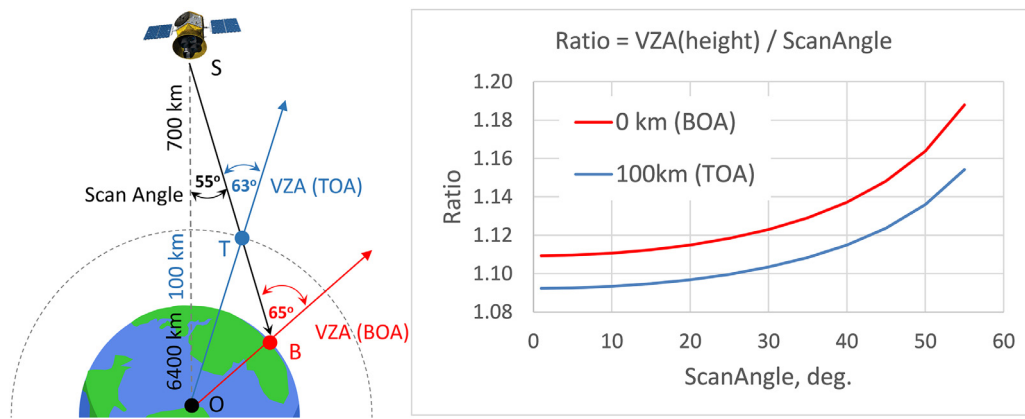


Fig. 2. In spherical geometry, the VZA for a point in atmosphere depends on the height (left image). For the NASA A-Train orbit at ~700 km, a scan angle of 55° between the satellite nadir SO and the view direction SB corresponds to VZA = 63° on TOA (point T) and VZA = 65° on BOA (point B). The right panel shows the ratio of the VZA to the scan angle at TOA and BOA. For a plane-parallel atmosphere, all VZAs would be 55°.

gle scattering. The work by Kalkofen, [40]: p.235, contains a section on “Spherical radiative transfer” (Chapter II), but this book is hard to find and, as of now, we have not been able to check for the availability of numerical data. In Part II of Lenoble, [49]: p.247, there is Chapter 3 “Spherical planetary atmospheres illuminated by the solar beam”, again with no numerical results. The same can be said for Section 10.11 “Numerical Results” in Natsuyama’s [61] Chapter 10 “Transfer of Radiation with Spherical Symmetry” –this contains only figures. In the book by Stamnes et al., [86]: Appendix M², there is a discussion on the influence of Earth curvature on the optical path and the Chapman function formalism [12]. The RT code DISORT [85] has used this technique for about three decades [37,55], however we are not aware of published numerical data from the DISORT team [47].

Years of intensive theoretical studies coupled with the easy availability of computational resources have resulted in the development of several true- and pseudo-spherical RT codes. Most, if not all, plane-parallel techniques have been extended to the spherical case. This includes the Monte Carlo method [1,5,7,11,13,15,25,27,29,31,32,62,63,66–69,81,97], discrete ordinates [2,12,16,17,24,73–75,82–84] including low number of streams approximation [46,90,94], two [60] and successive orders of scattering [6,21,43,59,87,96], Gauss-Seidel iterations [23,34,52], source integration for the first order of scattering [18,91–93], combined differential-integral approach [70–72], finite-difference and adding-doubling [33], invariant imbedding [3], Eddington [89], Picard iteration [19], small-angle modification [22], and Markov chain [95]. Only Monte Carlo models can simulate multiple scattering in true spherical geometry, while the other models can only offer corrections to the plane-parallel approach (pseudo-sphericity). The pseudo-spherical approach aims to deploy the numerical efficiency of plane-parallel codes to provide practical results of sufficient accuracy.

Some of these codes have been deployed in spherical RT model intercomparisons [9,36,39,51,64,65]. Contrary to situation with plane-parallel models, for which accurate benchmark data are available for a variety of scenarios, [10,26]; see also [44]: p.306, Table 1, for earlier references, these papers on spherical-model intercomparisons do not report numbers.

In addition to the field of Earth science, other disciplines have seen active publishing of numerical solutions to the transport equation in spherical geometry. Examples include astrophysics [39], planetary science [95], and neutron transport, [14]: p.146,

Chapter XI “The spherical harmonics method for spherical geometries”. In the latter field, accurate numerical data [30] is available but usually for isotropic scattering from an internal source. This is similar to the thermal RT regime in a spherical Earth atmosphere, which is outside the scope of the present paper.

In rare cases, numerical benchmark data are in fact available. The A & K, [1]: p.143, Table 1, paper reports intensity reflected from a spherical Rayleigh atmosphere, but results are limited to the principal plane. Soon after the initial A & K publication, Kattawar & Adams, [41]: p.440, Table 1, and Kattawar, [42]: p.63, Table 2, published results for aerosols with the Henyey-Greenstein phase functions (2 different asymmetry parameters $g = 0.5$ and 0.7 , principal plane only) and with Mie scattering optical inputs (ratio of single to multiple scattering and brightness temperature), respectively. Blättner, [5]: p.543, Table 3, also reported ratios of results using second-order scattering and multiple scattering to first-order scattering values. Wilson & Sen, [94]: p.409, Table 1, report approximate numerical results for a spherical atmosphere over a Lambertian surface, with comparisons to those obtained by Sobolev, [80]: p.231. Ding & Gordon [15] confirmed the hypothesis of Adams & Kattawar [1] that the multiple-to-single scattering ratio remains “sufficiently close” for the plane-parallel and spherical atmospheres in the principal plane. They also found that their numerical simulations agree with those in Adams & Kattawar [1] within 0.3% (p.7098). Spurr, [82]: p.155, Table 1, reports results for relative azimuth 60°. However, his test case input depends on the LOWTRAN atmospheric parameters, and cannot be easily reproduced, [82]: p.156, Section 6.1. The results of Postylaykov, [66]: p.310, Table 1, suffer from similar problem. Zhuravleva, [97]: p.7, Table 2, reports fluxes, which is not helpful for validation of solar-view dependency in backscatter intensity.

It is clear that our literature analysis confirms the need for additional publication of numerical benchmark results for spherical atmospheres. The next section explains the methodology for obtaining our benchmarks and provides estimations of their accuracy.

3. Methodology

3.1. Spherical atmosphere in MYSTIC and VLIDORT

The libRadtran’s Monte Carlo RT solver MYSTIC simulates various radiative quantities, e.g., radiances and irradiances, monochromatic or spectrally integrated. The observer position can be on a satellite, on the ground or in the atmosphere, e.g. on an air-plane. Per default, all scattering orders are simulated. For theoretical studies it is also possible to simulate individual scattering or-

² www.cambridge.org/stamnes or www.rtatmocrn.com (accessed June 12, 2020)

Table 1a
VZA at BOA as a function of VZA at TOA.

θ_{TOA} , degrees	θ_{BOA} , degrees
0	0.00
10	10.16
20	20.33
30	30.52
40	40.76
50	51.08
60	61.60
70	72.64

Table 1b
Same as Table 1a except for SZA and relative azimuth in the principal plane.

θ_{TOA}	θ_{BOA}	φ_{BOA}
#	$\theta_{\text{BOA}} = 0^\circ$	φ_{TOA}
0	0.00	180
10	0.16	180
20	0.33	180
30	0.52	180
40	0.76	180
50	1.08	180
60	1.60	180
70	2.64	180
#	$\theta_{\text{BOA}} = 70.47^\circ$	$\varphi_{\text{TOA}} = 0^\circ$
0	70.47	0
10	70.31	0
20	70.14	0
30	69.95	0
40	69.71	0
50	69.39	0
60	68.87	0
70	67.83	0
#	$\theta_{\text{BOA}} = 84.26^\circ$	$\varphi_{\text{TOA}} = 0^\circ$
0	84.26	0
10	84.10	0
20	83.93	0
30	83.74	0
40	83.50	0
50	83.18	0
60	82.66	0
70	81.62	0
#	$\theta_{\text{BOA}} = 70.47^\circ$	$\varphi_{\text{TOA}} = 180^\circ$
0	70.47	180
10	70.63	180
20	70.80	180
30	70.99	180
40	71.23	180
50	71.55	180
60	72.07	180
70	73.11	180
#	$\theta_{\text{BOA}} = 84.26^\circ$	$\varphi_{\text{TOA}} = 180^\circ$
0	84.26	180
10	84.42	180
20	84.59	180
30	84.78	180
40	85.02	180
50	85.34	180
60	85.86	180
70	86.90	180

Table 1c
Same as Table 1b but away from the principal plane.

θ_{TOA}	θ_{BOA}	φ_{BOA}
#	$\theta_{\text{BOA}} = 70.47^\circ$	$\varphi_{\text{TOA}} = 45^\circ$
0	70.47	45.00
10	70.36	45.04
20	70.24	45.08
30	70.10	45.13
40	69.93	45.19
50	69.71	45.28
60	69.35	45.41
70	68.62	45.70
#	$\theta_{\text{BOA}} = 84.26^\circ$	$\varphi_{\text{TOA}} = 45^\circ$
0	84.26	45.00
10	84.15	45.01
20	84.03	45.02
30	83.89	45.04
40	83.72	45.06
50	83.49	45.08
60	83.13	45.12
70	82.40	45.22
#	$\theta_{\text{BOA}} = 70.47^\circ$	$\varphi_{\text{TOA}} = 90^\circ$
0	70.47	90.00
10	70.47	90.06
20	70.47	90.12
30	70.47	90.18
40	70.47	90.27
50	70.47	90.38
60	70.48	90.57
70	70.49	90.94
#	$\theta_{\text{BOA}} = 84.26^\circ$	$\varphi_{\text{TOA}} = 90^\circ$
0	84.26	90.00
10	84.26	90.02
20	84.26	90.03
30	84.26	90.05
40	84.26	90.08
50	84.26	90.11
60	84.26	90.16
70	84.27	90.27
#	$\theta_{\text{BOA}} = 70.47^\circ$	$\varphi_{\text{TOA}} = 135^\circ$
0	70.47	135.00
10	70.58	135.04
20	70.70	135.08
30	70.84	135.13
40	71.01	135.19
50	71.24	135.27
60	71.60	135.39
70	72.35	135.62
#	$\theta_{\text{BOA}} = 84.26^\circ$	$\varphi_{\text{TOA}} = 135^\circ$
0	84.26	135.00
10	84.37	135.01
20	84.49	135.02
30	84.63	135.04
40	84.80	135.05
50	85.03	135.07
60	85.39	135.10
70	86.13	135.16

Large Telescope (ESO VLT) polarimetric earthshine observations in 2011 [28].

For reflectance, A & K [1] and MYSTIC define the solar-view geometry at TOA which is different from that of VLIDORT. This difference must be accounted for in the comparisons. We refer the reader to Appendix 1 for details of the TOA-BOA transformation of the solar-view geometry in the principal plane, and Appendix 2 in a general case. In addition, Appendix 3 describes an algorithm for computation of the relative azimuths located on the sunlit side of the Earth. This effect is included naturally in the full-spherical code. In addition to the Appendices, Table 1 contains numerical values of solar-view geometries used in this work: Table 1a – BOA VZA as a function of the TOA; Table 1b – same as (a) but for SZA

ders. The variance reduction technique [8] was turned on in all our simulations. Following Emde et al., [26]: p.12, we used 100M photons in the reported results. We configured other input parameters using the manual available from the libRadtran website. Emde & Mayer, [25]: p.2261, and Ockenfuß et al., [63]: p.4, briefly discuss the MYSTIC spherical geometry, in which a photon is traced “backward” from the detector to the source. In those papers, MYSTIC was tested against measurements taken during solar eclipses in the years 2006 and 2017. MYSTIC also allows to define a 3D spherical atmosphere. This option has been used to interpret the Very

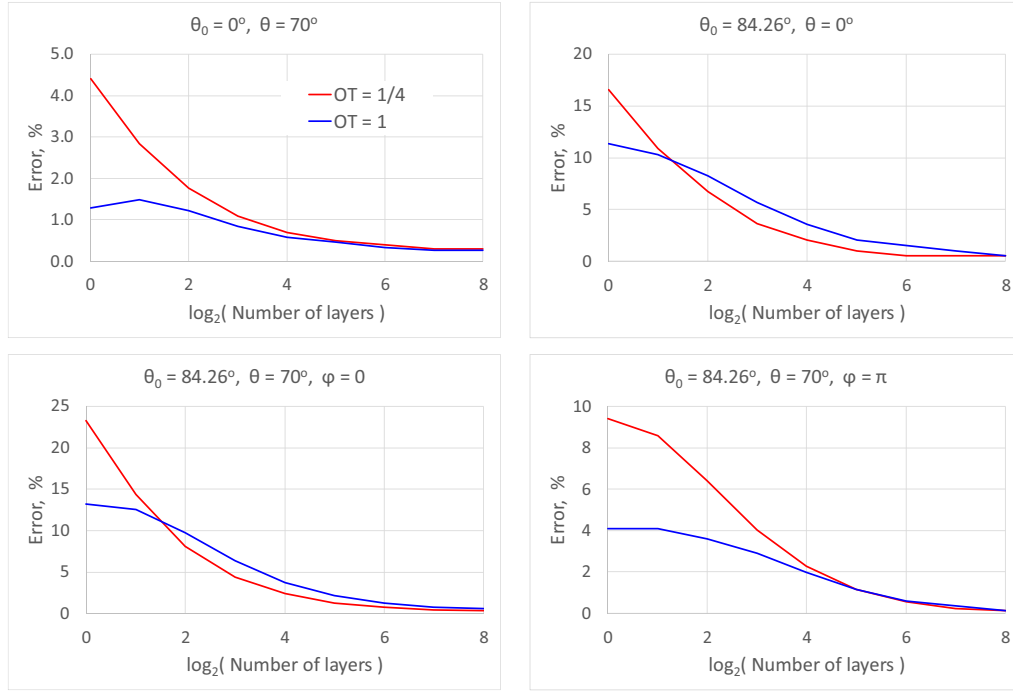


Fig. 3. Convergence of the single-scattering (SS) solution for different solar-view geometries (as indicated in panel titles) and optical thickness (OT) plotted against the number of layer elements. The scenario and the solar-view geometrical configuration are defined in A&K [1]; Table 1. The SS subroutine was developed to account for the effect of sphericity in the plane-parallel RT code IPOL [45].

and relative azimuth in the principal plane; Table 1c – same as (b) but away from the principal plane.

Note that a pseudo-spherical solver based on the RT code DIS-ORT [12] is also available in libRadtran. We do not include it in our benchmarks, due to relatively high reported error, ~5%–20%, depending on the solar-view geometry, see Abstracts in [9] and [34].

To increase accuracy of sphericity corrections within the framework of the multiple-scatter plane-parallel model, we adopt the following approach implemented in the new VLIDORT version 2.8.2. The single scattering (SS) radiation field is computed accurately in a spherical atmosphere using enough (~100) vertical layers (Fig. 3) to ensure a smooth variation of the solar and view angles along the LOS. For calculating multiple scattering (MS) radiation fields, the incident solar beam attenuation is calculated in a curved atmosphere as in the standard pseudo-spherical approximation. To allow for changes of geometry along the LOS, we run the MS computations twice: once for the TOA solar/view geometry configuration, and a second time with the BOA geometry. These two multiple scattering intensities (recall, we ignore polarization in this study) and a SS intensity, which is accurately known for a curved atmosphere, are used to build the upwelling intensity field in the atmosphere by source function integration, starting with the upwelling intensity at BOA. We now summarize this process.

At BOA, the VLIDORT calculation of upwelling intensity I_{surf} at the ground comprises two terms – the direct-bounce field I_{DB} from the accurate spherical SS code, and the diffuse-field multiple-scatter contribution I_{MB} :

$$I_{surf} = I_{DB} + I_{MB}. \quad (4)$$

Referring to the sketch in Fig. 1, when the LOS path traverses layer n in our curved atmosphere, the intensity I_{n-1} at the top of the layer is determined through source-function integration:

$$I_{n-1} = T_n I_n + S_n + M_n. \quad (5)$$

Here, the radiation field at layer bottom is I_n and T_n is the LOS transmittance. Terms S_n and M_n are the integrated SS and MS layer

source terms respectively. Eq. (5) is applied recursively along the LOS, starting with the BOA value I_{surf} , Eq. (4), at BOA and ending with the TOA radiation field I_0 at TOA.

The SS calculation based on the BOA geometrical configuration will deliver both the SS source term as well as the LOS transmittances T_n and S_n , along with the direct-bounce intensity at the surface I_{DB} ; as noted already, this calculation is accurate for spherical geometry. The total recursively developed TOA field is then given by

$$I_0 = (I_{DB} + I_{MB})C_N + \sum_{n=1}^N (S_n + M_n)C_{n-1}, \quad C_{n>0} = \prod_{k=1}^n T_k, \quad C_0 = 1. \quad (6)$$

The cumulative LOS transmittances are $\{C_n\}$, $n = 0, 1, \dots, N$. Here, N is the total number of layers.

The terms $\{M_n\}$, $n = 1, \dots, N$ are obtained as follows. The modified VLIDORT call will now supply I_{MB} (for the BOA-geometry configuration) and two sets $\{M_n^{(BOA)}\}$ and $\{M_n^{(TOA)}\}$ of multiple-scatter layer source terms from the two calculations with BOA and TOA geometries respectively. Next, these two sets of MS source terms are linearly interpolated against $\mu = \cos(\text{VZA})$ to find the changing value of M_n for each layer on the way from BOA to TOA. Although it is also possible to do this interpolation against $\mu_0 = \cos(\text{SZA})$ the interpolation against μ is free from ambiguities.

It should be noted that the diffuse-scattering surface intensity I_{MB} and the two sets of layer multiple-scattering source terms used in the source function integration are final values, after application of the cosine-azimuth summation of Fourier components of the intensity field.

We call this VLIDORT modification a “2-point sphericity correction”. This correction is more accurate compared to the previous pseudo spherical corrections that have been considered in LIDORT and VLIDORT [82–84]. The accuracy of the MS source term determination can be improved further by calling VLIDORT with 3 geometries, at BOA, TOA and one other pre-specified point along the

Table 2

Monte Carlo convergence rate, in%, for single (SS) and multiple (MS) scattering modes, Eq. (8).

τ	Scattering	max	average
0.25	SS	0.06	0.04
0.25	MS	0.08	0.05
1.0	SS	0.06	0.03
1.0	MS	0.06	0.03

LOS - this would be a “3-point sphericity correction”. An even better accuracy could be obtained by calling VLIDORT with a whole series of geometrical configurations at every boundary level between BOA and TOA (i.e., “multipoint sphericity correction”). Obviously the 2-point correction is the fastest to implement. Here we confine our attention to Rayleigh atmosphere, and consider only the 2-point corrections for VLIDORT in our comparisons with MYSTIC.

3.2. Accuracy of the results

MYSTIC is used in this paper as a baseline for our benchmarks. We have checked its convergence using the 3σ -rule (99.7% confidence) that estimates the relative accuracy of the Monte Carlo code as

$$I_{MC} = \tilde{I}_{MC} \pm 3\sigma, \quad (7)$$

where the mean intensity, \tilde{I}_{MC} , and the standard deviation, σ , are outputs from MYSTIC. We define the relative accuracy of the MC simulations according to

$$\varepsilon_{MC} = \frac{3\sigma}{\tilde{I}_{MC}} 100\%. \quad (8)$$

Following the recommendations in *Emde*, [26]: p.12, we used 100M photons for the computations.

Table 2 gives the maximum and average errors over all solar-view geometries for two optical depths, separately for single and multiple scattering, and according to the abovementioned criteria. The table shows with confidence that MYSTIC converges within a 0.1% error.

The accuracy of VLIDORT depends on three conditions: (i) a convergence criterion for the number of azimuthal (Fourier) expansion moments needed to compute the solution to a certain level accuracy; (ii) the number of polar discrete ordinates (quadrature streams) used to solve the plane-parallel integro-differential RT equations in each layer; and (iii) for a spherical atmosphere, the number of layers needed to account for smooth change of the solar-view geometry along the LOS (Fig. 3). For the pure Rayleigh scattering case, there are no Fourier convergence or discrete ordinates issues – the 3 azimuthal (Fourier) components were computed using 8 discrete ordinates in each polar hemisphere (16 streams in total). To ensure a smooth change of the solar-view geometry along the LOS, we executed VLIDORT with 100 layers and used control run with only 50 layers to ensure that the numerical uncertainty of this parameterization did not exceed 0.1%.

A & K do not provide explicit values of the standard deviation in their tabulated Monte Carlo results. However, they estimate the accuracy of their simulations for the *plane-parallel* case as follows (p.151). In SS the reciprocity principle, Eq. (3), is obeyed to within 3 significant digits; in MS – within 3%. For spherical atmospheres, they also provide SS numbers to 3 digits, which yields up to 0.3% (0.1% on average) and 0.5% (0.2% on average) for optical thickness $\tau = 0.25$ and 1.0, respectively, assuming that the round-off error dominates. For spherical geometry, A & K provide the SS/MS ratios using only 2 digits. Based on their accuracy estimations in the plane-parallel case, we set their relative accuracy for MS in spheri-

cal geometry to be 3%. It is worth noting that *Ding & Gordon*, [15]: p.7098, agreed with A & K to within 0.3%.

Finally, before running the spherical examples, we checked VLIDORT and MYSTIC for consistency in inputs and accuracy in output through use of the A & K plane-parallel scenario. In all the plane-parallel cases, VLIDORT and MYSTIC results agreed with those from A & K at ~2% or better, and between each other at 0.1% or better. Both these deviations are close to what we expect, given the accuracy of the A & K tables, the MYSTIC standard deviation, and the VLIDORT number of streams. In the next section, we report on numerical results suitable for benchmarking spherical RT codes.

4. Numerical results and discussion

Following A & K, we consider the diffuse upwelling reflectance from a spherical conservative Rayleigh scattering atmosphere of optical thicknesses $\tau = 0.25$ and 1 over a black surface. Polarization and ray bending due to refraction are ignored. For SS, A & K report results to 3 significant digits, which is accurate enough for practical needs, but insufficiently precise for numerical tests aiming at an error level of ~0.1%. For MS their results are less accurate: only 2 digits for the SS/MS scattering ratios. Therefore, we have reproduced their results with higher accuracy to provide a) 5 digits for both SS and MS, of which the latter suffers from round-off error; and b) absolute values for MS, instead of ratios.

Our results are grouped in Tables 3 and 4 for optical thickness 0.25 and 1.0. In each table, sections (a) and (b) correspond to SS and MS, respectively. We keep the appearance of our tables close to that for original tables by A & K. In Table 3a ($\tau = 0.25$, SS) the columns from left to right show: VZA at TOA, original results by A & K (except in exponential format), MYSTIC results, VLIDORT results, relative deviation of the A & K results vs. MYSTIC, relative deviation of VLIDORT results vs. MYSTIC. Tables 1a & b contain the solar-view geometry at BOA as input for VLIDORT. The VLIDORT's VZA at TOA is limited by the critical angle 79.9° (see the note in the Introduction). The solar (SZA) and azimuth (φ) angles at TOA go from top to bottom in the sequence defined by A & K. For SS at $\tau = 0.25$, the maximum and average deviations of the A & K results from MYSTIC turned out to be 0.32% and 0.11%, respectively (indicated at the bottom of the table). The same quantities for VLIDORT are 0.05% and 0.02%.

The TOA solar-view geometry in Table 3b ($\tau = 0.25$, MS) is organized as in Table 3a, but the sequence of columns is slightly different: VZA at TOA (left-most entry), SS by A & K, SS/MS ratio from A & K. This ratio is followed by absolute values of the MS not indicated in the original A & K's tables. The four columns on the right are the same as those in Table 3a. For MS at $\tau = 0.25$, the maximum and average deviations of the A & K results from MYSTIC turned out to be 4.7% and 1.2%, respectively. The same quantities for VLIDORT are 0.5% and 0.3%.

Tables 4a,b are identical to Tables 3a,b, respectively, but shows results for $\tau = 1$. For SS (Table 4a) the maximum and average deviations of the A & K results from MYSTIC were 0.72% and 0.17%, respectively. The same quantities for VLIDORT were 0.07% and 0.02%. For multiple scattering (Table 4b) those numbers are 5.6% and 1.4% (A & K), and 0.37% and 0.11% (VLIDORT).

Tables 5(ab) ($\tau = 0.25$) and Tables 6(ab) ($\tau = 1$) contain **new results** for configurations away from the principal plane for SS (a) and MS (b) scattering modes. The sequence of relative azimuths is $\varphi = 45^\circ, 90^\circ, 135^\circ$. In all the tables, the columns from left to right indicate the TOA VZA, followed by MYSTIC, VLIDORT, and percentile deviations of the two model results. At the bottom of each table, we record the maximum and average deviations computed over all solar-view geometries for a given OT and scattering mode.

Table 7 combines all the deviations together; this table should be read alongside Table 2 (accuracy of MYSTIC).

Table 3a

Reproduced results by A&K for SS and OT=0.25. Columns (left to right) show: TOA VZA, original results by A&K (except in exponential format), MYSTIC (MC) results, VLIDORT (VL) results, relative deviation of the A&K results vs MYSTIC, relative deviation of VLIDORT results vs MYSTIC. Maximum and average errors are indicated below, sign of errors ignored.

θ_{TOA}	A&K	MC	VL	A&K vs MC %	VL vs MC %
#		$\theta_{0,\text{TOA}} = 0^\circ$	φ_{TOA}		
0	7.38E-02	7.3785E-02	7.3776E-02	0.02	0.01
10	7.37E-02	7.3678E-02	7.3669E-02	0.03	0.01
20	7.35E-02	7.3420E-02	7.3442E-02	0.11	0.03
30	7.34E-02	7.3416E-02	7.3393E-02	0.02	0.03
40	7.41E-02	7.4131E-02	7.4135E-02	0.04	0.01
50	7.68E-02	7.6828E-02	7.6827E-02	0.04	0.00
60	8.40E-02	8.3928E-02	8.3945E-02	0.09	0.02
70	1.02E-01	1.0171E-01	1.0172E-01	0.29	0.01
80	1.72E-01	1.7215E-01		0.09	
85	1.71E-01	1.7132E-01		0.19	
88	1.26E-01	1.2623E-01		0.18	
#		$\theta_{0,\text{TOA}} = 70.47^\circ$	$\varphi_{\text{TOA}} = 0^\circ$		
0	3.33E-02	3.3331E-02	3.3331E-02	0.09	0.00
10	3.13E-02	3.1281E-02	3.1274E-02	0.06	0.02
20	3.18E-02	3.1804E-02	3.1804E-02	0.01	0.00
30	3.54E-02	3.5403E-02	3.5404E-02	0.01	0.00
40	4.30E-02	4.2963E-02	4.2979E-02	0.09	0.04
50	5.63E-02	5.6271E-02	5.6261E-02	0.05	0.02
60	7.92E-02	7.9092E-02	7.9117E-02	0.14	0.03
70	1.22E-01	1.2190E-01	1.2191E-01	0.08	0.01
80	2.54E-01	2.5377E-01		0.09	
85	2.94E-01	2.9408E-01		0.03	
88	2.33E-01	2.3252E-01		0.21	
#		$\theta_{0,\text{TOA}} = 84.26^\circ$	$\varphi_{\text{TOA}} = 0^\circ$		
0	1.93E-02	1.9258E-02	1.9261E-02	0.22	0.02
10	1.96E-02	1.9562E-02	1.9561E-02	0.20	0.00
20	2.17E-02	2.1662E-02	2.1674E-02	0.17	0.05
30	2.59E-02	2.5905E-02	2.5904E-02	0.02	0.00
40	3.29E-02	3.2888E-02	3.2892E-02	0.04	0.01
50	4.40E-02	4.3926E-02	4.3904E-02	0.17	0.05
60	6.21E-02	6.2019E-02	6.2043E-02	0.13	0.04
70	9.62E-02	9.6035E-02	9.6061E-02	0.17	0.03
80	2.10E-01	2.1001E-01		0.01	
85	2.79E-01	2.7884E-01		0.06	
88	2.39E-01	2.3945E-01		0.19	
#		$\theta_{0,\text{TOA}} = 70.47^\circ$	$\varphi_{\text{TOA}} = 180^\circ$		
0	3.34E-02	3.3336E-02	3.3331E-02	0.19	0.01
10	3.78E-02	3.7731E-02	3.7734E-02	0.18	0.01
20	4.45E-02	4.4451E-02	4.4442E-02	0.11	0.02
30	5.37E-02	5.3653E-02	5.3649E-02	0.09	0.01
40	6.60E-02	6.5919E-02	6.5927E-02	0.12	0.01
50	8.27E-02	8.2609E-02	8.2604E-02	0.11	0.01
60	1.07E-01	1.0681E-01	1.0682E-01	0.18	0.01
70	1.47E-01	1.4714E-01	1.4713E-01	0.09	0.00
80	2.50E-01	2.5012E-01		0.05	
85	3.00E-01	2.9989E-01		0.04	
88	2.37E-01	2.3719E-01		0.08	
#		$\theta_{0,\text{TOA}} = 84.26^\circ$	$\varphi_{\text{TOA}} = 180^\circ$		
0	1.93E-02	1.9258E-02	1.9261E-02	0.22	0.02
10	2.07E-02	2.0650E-02	2.0645E-02	0.24	0.02
20	2.38E-02	2.3725E-02	2.3719E-02	0.32	0.02
30	2.87E-02	2.8646E-02	2.8649E-02	0.19	0.01
40	3.59E-02	3.5818E-02	3.5821E-02	0.23	0.01
50	4.61E-02	4.6124E-02	4.6138E-02	0.05	0.03
60	6.15E-02	6.1527E-02	6.1530E-02	0.04	0.01
70	8.72E-02	8.7254E-02	8.7245E-02	0.06	0.01
80	1.41E-01	1.4091E-01		0.07	
85	2.00E-01	1.9995E-01		0.03	
88	2.31E-01	2.3099E-01		0.00	
MAX%				0.32	0.05
AVER%				0.11	0.02

Table 3b

Similar to Table 3a except for MS. Columns (left to right) show: TOA VZA, SS from A&K, SS/MS ratio from A&K, absolute values of the MS (not indicated in the original A&K tables). The four right-most columns are the same as those in Table 3a.

θ_{TOA}	A&K SS	A&K SS/MS%	A&K MS	MC	VL	A&K vs MC %	VL vs MC %
#			$\theta_{0,\text{TOA}} = 0^\circ$	$\varphi_{\text{TOA}} = 0^\circ$			
0	7.38E-02	82	9.00E-02	9.0710E-02	9.0779E-02	0.78	0.08
10	7.37E-02	81	9.10E-02	9.0930E-02	9.0985E-02	0.06	0.06
20	7.35E-02	80	9.19E-02	9.1661E-02	9.1731E-02	0.23	0.08
30	7.34E-02	80	9.18E-02	9.3326E-02	9.3439E-02	1.69	0.12
40	7.41E-02	76	9.75E-02	9.6852E-02	9.6981E-02	0.67	0.13
50	7.68E-02	74	1.04E-01	1.0391E-01	1.0404E-01	0.12	0.13
60	8.40E-02	70	1.20E-01	1.1806E-01	1.1828E-01	1.64	0.19
70	1.02E-01	67	1.52E-01	1.4869E-01	1.4912E-01	2.39	0.29
80	1.72E-01	67	2.57E-01	2.5879E-01		0.80	
85	1.71E-01	67	2.55E-01	2.5168E-01		1.41	
88	1.26E-01	72	1.75E-01	1.7773E-01		1.54	
#			$\theta_{0,\text{TOA}} = 70.47^\circ$	$\varphi_{\text{TOA}} = 0^\circ$			
0	3.33E-02	69	4.83E-02	4.8711E-02	4.8822E-02	0.92	0.23
10	3.13E-02	68	4.60E-02	4.6932E-02	4.7052E-02	1.92	0.26
20	3.18E-02	64	4.97E-02	4.8469E-02	4.8578E-02	2.52	0.23
30	3.54E-02	64	5.53E-02	5.3883E-02	5.4008E-02	2.65	0.23
40	4.30E-02	67	6.42E-02	6.4359E-02	6.4517E-02	0.28	0.24
50	5.63E-02	70	8.04E-02	8.2185E-02	8.2371E-02	2.14	0.23
60	7.92E-02	71	1.12E-01	1.1238E-01	1.1267E-01	0.74	0.26
70	1.22E-01	73	1.67E-01	1.6855E-01	1.6912E-01	0.84	0.34
80	2.54E-01	75	3.39E-01	3.4233E-01		1.07	
85	2.94E-01	78	3.77E-01	3.7844E-01		0.40	
88	2.33E-01	81	2.88E-01	2.8599E-01		0.58	
#			$\theta_{0,\text{TOA}} = 84.26^\circ$	$\varphi_{\text{TOA}} = 0^\circ$			
0	1.93E-02	68	2.84E-02	2.8873E-02	2.9016E-02	1.70	0.49
10	1.96E-02	67	2.93E-02	2.9437E-02	2.9576E-02	0.62	0.47
20	2.17E-02	67	3.24E-02	3.2263E-02	3.2412E-02	0.39	0.46
30	2.59E-02	72	3.60E-02	3.7741E-02	3.7915E-02	4.69	0.46
40	3.29E-02	70	4.70E-02	4.6720E-02	4.6928E-02	0.60	0.45
50	4.40E-02	74	5.95E-02	6.0849E-02	6.1098E-02	2.28	0.41
60	6.21E-02	74	8.39E-02	8.4091E-02	8.4469E-02	0.20	0.45
70	9.62E-02	76	1.27E-01	1.2777E-01	1.2842E-01	0.93	0.51
80	2.10E-01	77	2.73E-01	2.7563E-01		1.05	
85	2.79E-01	82	3.40E-01	3.4411E-01		1.12	
88	2.39E-01	86	2.78E-01	2.7977E-01		0.66	
#			$\theta_{0,\text{TOA}} = 70.47^\circ$	$\varphi_{\text{TOA}} = 180^\circ$			
0	3.34E-02	67	4.99E-02	4.8722E-02	4.8823E-02	2.32	0.21
10	3.78E-02	69	5.48E-02	5.3488E-02	5.3607E-02	2.42	0.22
20	4.45E-02	75	5.93E-02	6.1268E-02	6.1394E-02	3.16	0.21
30	5.37E-02	76	7.07E-02	7.2323E-02	7.2491E-02	2.30	0.23
40	6.60E-02	76	8.68E-02	8.7534E-02	8.7713E-02	0.79	0.20
50	8.27E-02	77	1.07E-01	1.0866E-01	1.0889E-01	1.16	0.21
60	1.07E-01	76	1.41E-01	1.3996E-01	1.4027E-01	0.59	0.22
70	1.47E-01	76	1.93E-01	1.9287E-01	1.9339E-01	0.29	0.27
80	2.50E-01	76	3.29E-01	3.3037E-01		0.43	
85	3.00E-01	79	3.80E-01	3.7920E-01		0.14	
88	2.37E-01	82	2.89E-01	2.8907E-01		0.02	
#			$\theta_{0,\text{TOA}} = 84.26^\circ$	$\varphi_{\text{TOA}} = 180^\circ$			
0	1.93E-02	67	2.88E-02	2.8866E-02	2.9016E-02	0.21	0.52
10	2.07E-02	67	3.09E-02	3.0413E-02	3.0566E-02	1.59	0.50
20	2.38E-02	70	3.40E-02	3.4066E-02	3.4243E-02	0.19	0.52
30	2.87E-02	73	3.93E-02	4.0087E-02	4.0276E-02	1.92	0.47
40	3.59E-02	74	4.85E-02	4.8934E-02	4.9177E-02	0.86	0.50
50	4.61E-02	75	6.15E-02	6.1830E-02	6.2124E-02	0.59	0.48
60	6.15E-02	76	8.09E-02	8.1259E-02	8.1587E-02	0.42	0.40
70	8.72E-02	78	1.12E-01	1.1378E-01	1.1407E-01	1.74	0.26
80	1.41E-01	77	1.83E-01	1.8016E-01		1.64	
85	2.00E-01	85	2.35E-01	2.4165E-01		2.63	
88	2.31E-01	88	2.63E-01	2.6380E-01		0.49	
#							
MAX%						4.69	0.52
AVER%						1.19	0.31

Table 4aSame as Table 3a, except for $\tau = 1.0$.

θ_{TOA}	A&K	MC	VL	A&K vs MC %	VL vs MC %
#		$\theta_{0, \text{TOA}} = 0^\circ$	φ_{TOA}		
0	1.62E-01	1.6211E-01	1.6213E-01	0.07	0.01
10	1.61E-01	1.6130E-01	1.6131E-01	0.18	0.01
20	1.59E-01	1.5900E-01	1.5900E-01	0.00	0.00
30	1.56E-01	1.5562E-01	1.5564E-01	0.24	0.01
40	1.52E-01	1.5204E-01	1.5203E-01	0.03	0.01
50	1.49E-01	1.4939E-01	1.4938E-01	0.26	0.00
60	1.50E-01	1.4951E-01	1.4951E-01	0.33	0.00
70	1.55E-01	1.5464E-01	1.5464E-01	0.24	0.00
80	1.67E-01	1.6643E-01		0.34	
85	1.76E-01	1.7613E-01		0.07	
88	1.82E-01	1.8197E-01		0.02	
#		$\theta_{0, \text{TOA}} = 70.47^\circ$	$\varphi_{\text{TOA}} = 0^\circ$		
0	5.22E-02	5.2141E-02	5.2148E-02	0.11	0.01
10	4.90E-02	4.8866E-02	4.8866E-02	0.28	0.00
20	4.95E-02	4.9411E-02	4.9404E-02	0.18	0.01
30	5.45E-02	5.4367E-02	5.4369E-02	0.25	0.00
40	6.49E-02	6.4761E-02	6.4758E-02	0.21	0.01
50	8.24E-02	8.2199E-02	8.2181E-02	0.25	0.02
60	1.10E-01	1.0969E-01	1.0970E-01	0.29	0.01
70	1.53E-01	1.5321E-01	1.5322E-01	0.14	0.00
80	2.27E-01	2.2629E-01		0.31	
85	2.84E-01	2.8409E-01		0.03	
88	3.27E-01	3.2691E-01		0.03	
#		$\theta_{0, \text{TOA}} = 84.26^\circ$	$\varphi_{\text{TOA}} = 0^\circ$		
0	1.94E-02	1.9304E-02	1.9302E-02	0.50	0.01
10	1.97E-02	1.9559E-02	1.9569E-02	0.72	0.05
20	2.17E-02	2.1609E-02	2.1620E-02	0.42	0.05
30	2.59E-02	2.5726E-02	2.5718E-02	0.68	0.03
40	3.26E-02	3.2440E-02	3.2433E-02	0.49	0.02
50	4.30E-02	4.2827E-02	4.2802E-02	0.41	0.06
60	5.96E-02	5.9317E-02	5.9353E-02	0.48	0.06
70	8.85E-02	8.8201E-02	8.8227E-02	0.34	0.03
80	1.52E-01	1.5203E-01		0.02	
85	2.27E-01	2.2708E-01		0.01	
88	3.12E-01	3.1239E-01		0.00	
#		$\theta_{0, \text{TOA}} = 70.47^\circ$	$\varphi_{\text{TOA}} = 180^\circ$		
0	5.21E-02	5.2142E-02	5.2149E-02	0.08	0.01
10	5.89E-02	5.8868E-02	5.8862E-02	0.05	0.01
20	6.88E-02	6.8801E-02	6.8809E-02	0.00	0.01
30	8.20E-02	8.1990E-02	8.1999E-02	0.01	0.01
40	9.87E-02	9.8735E-02	9.8722E-02	0.04	0.01
50	1.20E-01	1.1984E-01	1.1983E-01	0.14	0.00
60	1.47E-01	1.4717E-01	1.4717E-01	0.12	0.00
70	1.85E-01	1.8501E-01	1.8502E-01	0.01	0.00
80	2.45E-01	2.4468E-01		0.13	
85	2.94E-01	2.9359E-01		0.14	
88	3.32E-01	3.3231E-01		0.09	
#		$\theta_{0, \text{TOA}} = 84.26^\circ$	$\varphi_{\text{TOA}} = 180^\circ$		
0	1.93E-02	1.9299E-02	1.9302E-02	0.00	0.01
10	2.07E-02	2.0702E-02	2.0704E-02	0.01	0.01
20	2.38E-02	2.3789E-02	2.3785E-02	0.05	0.02
30	2.87E-02	2.8704E-02	2.8708E-02	0.01	0.01
40	3.58E-02	3.5825E-02	3.5821E-02	0.07	0.01
50	4.60E-02	4.5964E-02	4.5996E-02	0.08	0.07
60	6.10E-02	6.1032E-02	6.0999E-02	0.05	0.05
70	8.58E-02	8.5844E-02	8.5833E-02	0.05	0.01
80	1.38E-01	1.3812E-01		0.08	
85	2.00E-01	2.0053E-01		0.26	
88	2.92E-01	2.9182E-01		0.06	
MAX%				0.72	0.07
AVER%				0.17	0.02

Table 4bSame as Table 3b, except for $\tau = 1.0$.

θ_{TOA}	A&K SS	A&K SS/MS%	A&K MS	MC	VL	A&K vs MC %	VL vs MC %
#			$\theta_{0, \text{TOA}} = 0^\circ$	φ_{TOA}			
0	1.62E-01	53	3.06E-01	3.0752E-01	3.0754E-01	0.60	0.01
10	1.61E-01	54	2.98E-01	3.0836E-01	3.0839E-01	3.31	0.01
20	1.59E-01	51	3.12E-01	3.1111E-01	3.1120E-01	0.21	0.03
30	1.56E-01	49	3.18E-01	3.1659E-01	3.1663E-01	0.56	0.01
40	1.52E-01	47	3.23E-01	3.2585E-01	3.2592E-01	0.75	0.02
50	1.49E-01	43	3.47E-01	3.4055E-01	3.4070E-01	1.75	0.05
60	1.50E-01	40	3.75E-01	3.6243E-01	3.6273E-01	3.47	0.08
70	1.55E-01	39	3.97E-01	3.8991E-01	3.9110E-01	1.93	0.31
80	1.67E-01	42	3.98E-01	4.0614E-01		2.10	
85	1.76E-01	44	4.00E-01	3.9747E-01		0.64	
88	1.82E-01	49	3.71E-01	3.7759E-01		1.63	
#			$\theta_{0, \text{TOA}} = 70.47^\circ$	$\varphi_{\text{TOA}} = 0^\circ$			
0	5.22E-02	38	1.37E-01	1.3215E-01	1.3212E-01	3.95	0.03
10	4.90E-02	37	1.32E-01	1.2997E-01	1.2993E-01	1.89	0.04
20	4.95E-02	38	1.30E-01	1.3393E-01	1.3388E-01	2.74	0.04
30	5.45E-02	38	1.43E-01	1.4493E-01	1.4482E-01	1.04	0.07
40	6.49E-02	39	1.66E-01	1.6422E-01	1.6417E-01	1.33	0.03
50	8.24E-02	42	1.96E-01	1.9412E-01	1.9407E-01	1.06	0.03
60	1.10E-01	47	2.34E-01	2.3816E-01	2.3830E-01	1.73	0.06
70	1.53E-01	51	3.00E-01	3.0167E-01	3.0250E-01	0.55	0.28
80	2.27E-01	57	3.98E-01	3.8969E-01		2.20	
85	2.84E-01	65	4.37E-01	4.4304E-01		1.38	
88	3.27E-01	71	4.61E-01	4.6949E-01		1.90	
#			$\theta_{0, \text{TOA}} = 84.26^\circ$	$\varphi_{\text{TOA}} = 0^\circ$			
0	1.94E-02	41	4.73E-02	4.6182E-02	4.6084E-02	2.46	0.21
10	1.97E-02	42	4.69E-02	4.7059E-02	4.6982E-02	0.33	0.16
20	2.17E-02	44	4.93E-02	5.0595E-02	5.0525E-02	2.52	0.14
30	2.59E-02	48	5.40E-02	5.7169E-02	5.7091E-02	5.62	0.14
40	3.26E-02	49	6.65E-02	6.7576E-02	6.7527E-02	1.55	0.07
50	4.30E-02	51	8.43E-02	8.3321E-02	8.3204E-02	1.19	0.14
60	5.96E-02	56	1.06E-01	1.0736E-01	1.0746E-01	0.87	0.09
70	8.85E-02	60	1.48E-01	1.4695E-01	1.4749E-01	0.38	0.37
80	1.52E-01	68	2.24E-01	2.2435E-01		0.37	
85	2.27E-01	75	3.03E-01	3.0495E-01		0.70	
88	3.12E-01	82	3.81E-01	3.8657E-01		1.45	
#			$\theta_{0, \text{TOA}} = 70.47^\circ$	$\varphi_{\text{TOA}} = 180^\circ$			
0	5.21E-02	40	1.30E-01	1.3217E-01	1.3212E-01	1.45	0.04
10	5.89E-02	43	1.37E-01	1.4004E-01	1.3997E-01	2.19	0.05
20	6.88E-02	45	1.53E-01	1.5335E-01	1.5329E-01	0.30	0.03
30	8.20E-02	48	1.71E-01	1.7226E-01	1.7226E-01	0.83	0.00
40	9.87E-02	50	1.97E-01	1.9741E-01	1.9740E-01	0.01	0.01
50	1.20E-01	52	2.31E-01	2.2996E-01	2.2997E-01	0.35	0.01
60	1.47E-01	53	2.77E-01	2.7201E-01	2.7204E-01	1.97	0.01
70	1.85E-01	56	3.30E-01	3.2695E-01	3.2715E-01	1.04	0.06
80	2.45E-01	62	3.95E-01	3.9881E-01		0.91	
85	2.94E-01	66	4.45E-01	4.4428E-01		0.26	
88	3.32E-01	71	4.68E-01	4.6891E-01		0.28	
#			$\theta_{0, \text{TOA}} = 84.26^\circ$	$\varphi_{\text{TOA}} = 180^\circ$			
0	1.93E-02	43	4.49E-02	4.6179E-02	4.6085E-02	2.80	0.20
10	2.07E-02	44	4.70E-02	4.7774E-02	4.7656E-02	1.53	0.25
20	2.38E-02	46	5.17E-02	5.1865E-02	5.1701E-02	0.24	0.32
30	2.87E-02	49	5.86E-02	5.8587E-02	5.8442E-02	0.03	0.25
40	3.58E-02	53	6.75E-02	6.8463E-02	6.8293E-02	1.34	0.25
50	4.60E-02	55	8.36E-02	8.2494E-02	8.2354E-02	1.38	0.17
60	6.10E-02	59	1.03E-01	1.0276E-01	1.0251E-01	0.61	0.25
70	8.58E-02	63	1.36E-01	1.3436E-01	1.3397E-01	1.36	0.29
80	1.38E-01	71	1.94E-01	1.9475E-01		0.20	
85	2.00E-01	77	2.60E-01	2.6124E-01		0.58	
88	2.92E-01	83	3.52E-01	3.5258E-01		0.22	
#							
MAX%						5.62	0.37
AVER%						1.35	0.11

Table 5a

New results for SS away from the principal plane, $\tau = 0.25$. Columns (left to right) show: TOA VZA, followed by MYSTIC (MC), VLIDORT (VL), and relative deviations of the two. The sequence of TOA relative azimuths (top to bottom) is $\varphi = 45^\circ, 90^\circ, 135^\circ$.

θ_{TOA}	MC	VL	[VL vs MC]%
#	$\theta_{0, \text{TOA}} = 70.47^\circ$	$\varphi_{\text{TOA}} = 45^\circ$	
0	3.3338E-02	3.3331E-02	0.02
10	3.1814E-02	3.1813E-02	0.00
20	3.2010E-02	3.2011E-02	0.00
30	3.4297E-02	3.4297E-02	0.00
40	3.9359E-02	3.9365E-02	0.02
50	4.8555E-02	4.8547E-02	0.02
60	6.4791E-02	6.4804E-02	0.02
70	9.5982E-02	9.5984E-02	0.00
80	1.9370E-01		
85	2.2488E-01		
88	1.7797E-01		
#	$\theta_{0, \text{TOA}} = 84.26^\circ$	$\varphi_{\text{TOA}} = 45^\circ$	
0	1.9262E-02	1.9261E-02	0.01
10	1.9432E-02	1.9427E-02	0.02
20	2.0795E-02	2.0798E-02	0.01
30	2.3598E-02	2.3600E-02	0.01
40	2.8277E-02	2.8291E-02	0.05
50	3.5815E-02	3.5820E-02	0.01
60	4.8371E-02	4.8396E-02	0.05
70	7.2312E-02	7.2307E-02	0.01
80	1.5171E-01		
85	2.0564E-01		
88	1.7939E-01		
#	$\theta_{0, \text{TOA}} = 70.47^\circ$	$\varphi_{\text{TOA}} = 90^\circ$	
0	3.3332E-02	3.3331E-02	0.00
10	3.3695E-02	3.3695E-02	0.00
20	3.4854E-02	3.4846E-02	0.02
30	3.7000E-02	3.6989E-02	0.03
40	4.0571E-02	4.0563E-02	0.02
50	4.6440E-02	4.6433E-02	0.01
60	5.6542E-02	5.6544E-02	0.00
70	7.6066E-02	7.6066E-02	0.00
80	1.3795E-01		
85	1.5866E-01		
88	1.2451E-01		
#	$\theta_{0, \text{TOA}} = 84.26^\circ$	$\varphi_{\text{TOA}} = 90^\circ$	
0	1.9264E-02	1.9261E-02	0.01
10	1.9528E-02	1.9530E-02	0.01
20	2.0368E-02	2.0374E-02	0.03
30	2.1924E-02	2.1927E-02	0.01
40	2.4470E-02	2.4476E-02	0.03
50	2.8604E-02	2.8600E-02	0.01
60	3.5621E-02	3.5628E-02	0.02
70	4.9174E-02	4.9162E-02	0.02
80	9.0296E-02		
85	1.2919E-01		
88	1.1919E-01		
#	$\theta_{0, \text{TOA}} = 70.47^\circ$	$\varphi_{\text{TOA}} = 135^\circ$	
0	3.3340E-02	3.3331E-02	0.03
10	3.6389E-02	3.6386E-02	0.01
20	4.0953E-02	4.0959E-02	0.01
30	4.7221E-02	4.7218E-02	0.01
40	5.5640E-02	5.5650E-02	0.02
50	6.7307E-02	6.7314E-02	0.01
60	8.4707E-02	8.4725E-02	0.02
70	1.1465E-01	1.1462E-01	0.03
80	1.9707E-01		
85	2.3109E-01		
88	1.8140E-01		
#	$\theta_{0, \text{TOA}} = 84.26^\circ$	$\varphi_{\text{TOA}} = 135^\circ$	
0	1.9268E-02	1.9261E-02	0.03
10	2.0205E-02	2.0206E-02	0.00
20	2.2271E-02	2.2274E-02	0.01
30	2.5606E-02	2.5603E-02	0.01
40	3.0547E-02	3.0539E-02	0.03
50	3.7810E-02	3.7798E-02	0.03
60	4.9031E-02	4.9035E-02	0.01
70	6.8546E-02	6.8549E-02	0.00
80	1.1351E-01		
85	1.6542E-01		
88	1.7560E-01		
#			
MAX%			0.05
AVER%			0.02

Table 5b

Same as Table 5a, except for MS.

θ_{TOA}	MC	VL	[VL vs MC]%
#	$\theta_{0, \text{TOA}} = 70.47^\circ$	$\varphi_{\text{TOA}} = 45^\circ$	
0	4.8720E-02	4.8822E-02	0.21
10	4.7458E-02	4.7587E-02	0.27
20	4.8618E-02	4.8741E-02	0.25
30	5.2649E-02	5.2776E-02	0.24
40	6.0484E-02	6.0644E-02	0.26
50	7.3983E-02	7.4194E-02	0.28
60	9.7304E-02	9.7571E-02	0.27
70	1.4129E-01	1.4184E-01	0.39
80	2.7906E-01		
85	3.0631E-01		
88	2.2969E-01		
#	$\theta_{0, \text{TOA}} = 84.26^\circ$	$\varphi_{\text{TOA}} = 45^\circ$	
0	2.8871E-02	2.9016E-02	0.50
10	2.9270E-02	2.9415E-02	0.49
20	3.1302E-02	3.1454E-02	0.48
30	3.5272E-02	3.5447E-02	0.49
40	4.1790E-02	4.2027E-02	0.56
50	5.2253E-02	5.2511E-02	0.49
60	6.9587E-02	6.9956E-02	0.53
70	1.0250E-01	1.0308E-01	0.57
80	2.1262E-01		
85	2.6667E-01		
88	2.1752E-01		
#	$\theta_{0, \text{TOA}} = 70.47^\circ$	$\varphi_{\text{TOA}} = 90^\circ$	
0	4.8725E-02	4.8823E-02	0.20
10	4.9369E-02	4.9486E-02	0.24
20	5.1457E-02	5.1570E-02	0.22
30	5.5235E-02	5.5392E-02	0.28
40	6.1462E-02	6.1636E-02	0.28
50	7.1460E-02	7.1661E-02	0.28
60	8.8268E-02	8.8524E-02	0.29
70	1.1988E-01	1.2042E-01	0.45
80	2.1880E-01		
85	2.3630E-01		
88	1.7418E-01		
#	$\theta_{0, \text{TOA}} = 84.26^\circ$	$\varphi_{\text{TOA}} = 90^\circ$	
0	2.8867E-02	2.9016E-02	0.51
10	2.9323E-02	2.9474E-02	0.51
20	3.0763E-02	3.0910E-02	0.47
30	3.3346E-02	3.3529E-02	0.55
40	3.7572E-02	3.7774E-02	0.53
50	4.4283E-02	4.4541E-02	0.58
60	5.5520E-02	5.5880E-02	0.64
70	7.6798E-02	7.7330E-02	0.69
80	1.4128E-01		
85	1.8190E-01		
88	1.5386E-01		
#	$\theta_{0, \text{TOA}} = 70.47^\circ$	$\varphi_{\text{TOA}} = 135^\circ$	
0	4.8701E-02	4.8823E-02	0.25
10	5.2132E-02	5.2229E-02	0.19
20	5.7678E-02	5.7816E-02	0.24
30	6.5726E-02	6.5865E-02	0.21
40	7.6942E-02	7.7106E-02	0.21
50	9.2890E-02	9.3090E-02	0.22
60	1.1713E-01	1.1744E-01	0.27
70	1.5936E-01	1.5984E-01	0.30
80	2.7701E-01		
85	3.0915E-01		
88	2.3206E-01		
#	$\theta_{0, \text{TOA}} = 84.26^\circ$	$\varphi_{\text{TOA}} = 135^\circ$	
0	2.8869E-02	2.9016E-02	0.50
10	2.9955E-02	3.0131E-02	0.58
20	3.2613E-02	3.2785E-02	0.52
30	3.6990E-02	3.7177E-02	0.50
40	4.3575E-02	4.3797E-02	0.51
50	5.3395E-02	5.3639E-02	0.45
60	6.8633E-02	6.8969E-02	0.49
70	9.5135E-02	9.5542E-02	0.43
80	1.5549E-01		
85	2.1035E-01		
88	2.0870E-01		
#			
MAX%			0.69
AVER%			0.39

Table 6a

Same as Table 5a, except for OT=1.0.

θ_{TOA}	MC	VL	VL vs MC %
#	$\theta_{0, \text{TOA}} = 70.47^\circ$	$\varphi_{\text{TOA}} = 45^\circ$	
0	5.2144E-02	5.2148E-02	0.01
10	4.9700E-02	4.9693E-02	0.01
20	4.9697E-02	4.9699E-02	0.01
30	5.2638E-02	5.2635E-02	0.01
40	5.9255E-02	5.9260E-02	0.01
50	7.0845E-02	7.0835E-02	0.01
60	8.9741E-02	8.9747E-02	0.01
70	1.2059E-01	1.2059E-01	0.00
80	1.7400E-01		
85	2.1737E-01		
88	2.5008E-01		
#	$\theta_{0, \text{TOA}} = 84.26^\circ$	$\varphi_{\text{TOA}} = 45^\circ$	
0	1.9299E-02	1.9302E-02	0.01
10	1.9445E-02	1.9438E-02	0.04
20	2.0759E-02	2.0756E-02	0.02
30	2.3440E-02	2.3461E-02	0.09
40	2.7940E-02	2.7947E-02	0.03
50	3.5009E-02	3.5023E-02	0.04
60	4.6449E-02	4.6470E-02	0.05
70	6.6867E-02	6.6852E-02	0.02
80	1.1277E-01		
85	1.6791E-01		
88	2.3311E-01		
#	$\theta_{0, \text{TOA}} = 70.47^\circ$	$\varphi_{\text{TOA}} = 90^\circ$	
0	5.2143E-02	5.2148E-02	0.01
10	5.2606E-02	5.2605E-02	0.00
20	5.4040E-02	5.4041E-02	0.00
30	5.6674E-02	5.6669E-02	0.01
40	6.0920E-02	6.0926E-02	0.01
50	6.7579E-02	6.7586E-02	0.01
60	7.8124E-02	7.8125E-02	0.00
70	9.5537E-02	9.5544E-02	0.01
80	1.2692E-01		
85	1.5378E-01		
88	1.7472E-01		
#	$\theta_{0, \text{TOA}} = 84.26^\circ$	$\varphi_{\text{TOA}} = 90^\circ$	
0	1.9298E-02	1.9302E-02	0.02
10	1.9563E-02	1.9561E-02	0.01
20	2.0376E-02	2.0374E-02	0.01
30	2.1868E-02	2.1863E-02	0.02
40	2.4278E-02	2.4286E-02	0.03
50	2.8156E-02	2.8155E-02	0.00
60	3.4591E-02	3.4598E-02	0.02
70	4.6448E-02	4.6422E-02	0.06
80	7.3936E-02		
85	1.0824E-01		
88	1.5321E-01		
#	$\theta_{0, \text{TOA}} = 70.47^\circ$	$\varphi_{\text{TOA}} = 135^\circ$	
0	5.2145E-02	5.2148E-02	0.01
10	5.6768E-02	5.6777E-02	0.02
20	6.3459E-02	6.3451E-02	0.01
30	7.2223E-02	7.2216E-02	0.01
40	8.3399E-02	8.3404E-02	0.01
50	9.7734E-02	9.7737E-02	0.00
60	1.1681E-01	1.1683E-01	0.01
70	1.4406E-01	1.4405E-01	0.00
80	1.8845E-01		
85	2.2532E-01		
88	2.5428E-01		
#	$\theta_{0, \text{TOA}} = 84.26^\circ$	$\varphi_{\text{TOA}} = 135^\circ$	
0	1.9302E-02	1.9302E-02	0.00
10	2.0247E-02	2.0260E-02	0.06
20	2.2316E-02	2.2322E-02	0.03
30	2.5619E-02	2.5613E-02	0.02
40	3.0470E-02	3.0460E-02	0.03
50	3.7539E-02	3.7519E-02	0.05
60	4.8275E-02	4.8293E-02	0.04
70	6.6561E-02	6.6553E-02	0.01
80	1.0617E-01		
85	1.5427E-01		
88	2.2294E-01		
#			
MAX%			0.09
AVER%			0.02

Table 6bSame as Table 5b, except for $\tau = 1.0$.

θ_{TOA}	MC	VL	VL vs MC %
#	$\theta_{0, \text{TOA}} = 70.47^\circ$	$\varphi_{\text{TOA}} = 45^\circ$	
0	1.3213E-01	1.3212E-01	0.01
10	1.3077E-01	1.3071E-01	0.05
20	1.3408E-01	1.3399E-01	0.06
30	1.4270E-01	1.4267E-01	0.02
40	1.5786E-01	1.5787E-01	0.00
50	1.8141E-01	1.8134E-01	0.04
60	2.1605E-01	2.1614E-01	0.04
70	2.6581E-01	2.6657E-01	0.28
80	3.3318E-01		
85	3.7201E-01		
88	3.8894E-01		
#	$\theta_{0, \text{TOA}} = 84.26^\circ$	$\varphi_{\text{TOA}} = 45^\circ$	
0	4.6195E-02	4.6084E-02	0.24
10	4.6864E-02	4.6752E-02	0.24
20	4.9525E-02	4.9430E-02	0.19
30	5.4521E-02	5.4443E-02	0.14
40	6.2441E-02	6.2374E-02	0.11
50	7.4442E-02	7.4386E-02	0.08
60	9.2827E-02	9.2855E-02	0.03
70	1.2300E-01	1.2334E-01	0.27
80	1.8117E-01		
85	2.4139E-01		
88	3.0347E-01		
#	$\theta_{0, \text{TOA}} = 70.47^\circ$	$\varphi_{\text{TOA}} = 90^\circ$	
0	1.3213E-01	1.3212E-01	0.01
10	1.3365E-01	1.3360E-01	0.04
20	1.3821E-01	1.3817E-01	0.03
30	1.4627E-01	1.4624E-01	0.03
40	1.5858E-01	1.5857E-01	0.01
50	1.7638E-01	1.7639E-01	0.01
60	2.0152E-01	2.0164E-01	0.06
70	2.3631E-01	2.3689E-01	0.25
80	2.8002E-01		
85	3.0258E-01		
88	3.0867E-01		
#	$\theta_{0, \text{TOA}} = 84.26^\circ$	$\varphi_{\text{TOA}} = 90^\circ$	
0	4.6193E-02	4.6084E-02	0.24
10	4.6799E-02	4.6709E-02	0.19
20	4.8750E-02	4.8643E-02	0.22
30	5.2198E-02	5.2095E-02	0.20
40	5.7598E-02	5.7486E-02	0.19
50	6.5700E-02	6.5592E-02	0.16
60	7.8053E-02	7.7971E-02	0.11
70	9.7934E-02	9.7932E-02	0.00
80	1.3531E-01		
85	1.7406E-01		
88	2.1719E-01		
#	$\theta_{0, \text{TOA}} = 70.47^\circ$	$\varphi_{\text{TOA}} = 135^\circ$	
0	1.3214E-01	1.3212E-01	0.02
10	1.3788E-01	1.3784E-01	0.03
20	1.4778E-01	1.4777E-01	0.00
30	1.6215E-01	1.6211E-01	0.03
40	1.8154E-01	1.8148E-01	0.03
50	2.0703E-01	2.0701E-01	0.01
60	2.4061E-01	2.4069E-01	0.03
70	2.8480E-01	2.8507E-01	0.10
80	3.4116E-01		
85	3.7422E-01		
88	3.8895E-01		
#	$\theta_{0, \text{TOA}} = 84.26^\circ$	$\varphi_{\text{TOA}} = 135^\circ$	
0	4.6197E-02	4.6085E-02	0.24
10	4.7364E-02	4.7276E-02	0.18
20	5.0424E-02	5.0328E-02	0.19
30	5.5579E-02	5.5418E-02	0.29
40	6.3197E-02	6.3017E-02	0.28
50	7.4178E-02	7.3973E-02	0.28
60	9.0271E-02	9.0085E-02	0.21
70	1.1555E-01	1.1528E-01	0.24
80	1.6362E-01		
85	2.1586E-01		
88	2.8408E-01		
#			
MAX%			0.29
AVER%			0.12

Table 7

Maximum and average deviations for MYSTIC and VLIDORT, in %, for single (SS) and multiple (MS) scattering modes computed over all solar-view geometries off the principal plane (new benchmark results).

Scattering mode: τ	Single scattering maximum	Single scattering average	Multiple scattering maximum	Multiple scattering average
0.25	0.05	0.02	0.69	0.39
1.0	0.09	0.02	0.29	0.12

5. Summary

The need for accurate spherical RT (O-RT) codes, e.g., for remote sensing of the Earth's atmosphere from a geostationary orbit at dusk and dawn, or Lagrange L1 orbit, or remote sensing of Polar regions, has been growing fast, along with the requirement for comprehensive accurate benchmarks. In this paper, we have reproduced and extended results from Adams & Kattawar [1] (A & K) for monochromatic solar light reflected from the top of the Earth's spherical atmosphere. In contrast to graphical figures frequently published in the literature, our numerical results are suitable for accurate benchmarking of the O-RT codes.

Our Tables 3–6 report numerical results for unpolarized light reflected from the top of a Rayleigh scattering atmosphere over a black surface, for two optical thicknesses (0.25 and 1.0), for both single and multiple scattering, in and out of the principal plane using two state-of-the-art RT codes: libRadtran's MYSTIC (Monte Carlo) and VLIDORT (discrete ordinates). The two codes agreed perfectly (within 0.1%) for single scattering and within 0.7% (0.4% on average) for multiple scattering (Table 7).

However, this paper only partially fills the gap in O-RT benchmarking. Benchmark results for polarization, transmitted radiation, limb observations, reflecting surface, aerosol and absorption profiles, high cirrus clouds, and refraction among other effects are yet to be generated and tested.

Author statement

Sergey Korkin: Original manuscript preparation, MYSTIC simulations.

Eun-Su Yang: VLIDORT simulations, error analysis.

Robert Spurr: developer of VLIDORT RT code including 2-, 3-, and multipoint spherical corrections.

Claudia Emde: co-developer and support of libRadtran's MYSTIC RT code.

Nickolay Krotkov: Conceptualization, Funding acquisition.

Alexander Vasilkov: Conceptualization, Funding acquisition.

David Haffner: Formal analysis.

Jungbin Mok: VLIDORT simulations, error analysis.

Alexei Lyapustin: Conceptualization, Funding acquisition.

All: manuscript discussion, review & editing, reply to reviewers.

Declaration of Competing Interest

Authors of this manuscript declare no conflicts of interests.

Acknowledgments

The work of S. Korkin was supported by the NASA's Earth Science Division under Grant 17-TASNPP17-0116, and in part by the USRA Internal Research & Development (R&D) program. He is also thankful to James Limbacher (SSAI and NASA GSFC) for discussion of many related topics from RT and Monte Carlo, to parallel computing in Python, and to Corey Bettenhausen (Adnet and NASA GSFC) for help with libRadtran setup. We are grateful to three anonymous reviewers for their comments and suggestions.

Appendix 1: Transformation of the Solar-View Geometry from TOA to BOA in the Principal Plane

Here we derive the solar-view geometry at BOA from the one at TOA in the principal plane. VLIDORT uses the BOA geometry as the baseline, while A & K and MYSTIC use the TOA configuration.

Fig. 4 shows several solar beam directions for a given LOS (view direction). The relative TOA azimuth, $\varphi_{TOA} = 0^\circ$, corresponds to forward scattering.

The TOA-to-BOA computation of the VZA at BOA uses the sine-rule relation, Eq. (1). We get the solar zenith angle at BOA depending on the TOA input as described below. We assume $\varphi_{BOA} = \varphi_{TOA}$ if the BOA azimuth is undefined.

Case 1: $\varphi_{TOA} = 0^\circ$, Fig. 4(a). The “red” solar beam is a limiting case for the “green” one: $\theta_{0,BOA} = 0^\circ$, φ_{BOA} is not defined, $\theta_{0,TOA}^{Critical} = \theta_{BOA} - \theta_{TOA}$ is a critical value. For $\theta_{0,TOA} < \theta_{0,TOA}^{Critical}$, the relative azimuths at TOA & BOA differ; otherwise, the azimuth is preserved. Both VZAs are known from the sine-rule relation, $\theta_{BOA} > \theta_{TOA}$. For the “green” solar beam: $\varphi_{BOA} = 0^\circ$; $\theta_{0,TOA} + \theta_{TOA} = \theta_{0,BOA} + \theta_{BOA}$. For the “blue” solar beam: $\theta_{0,TOA} <$

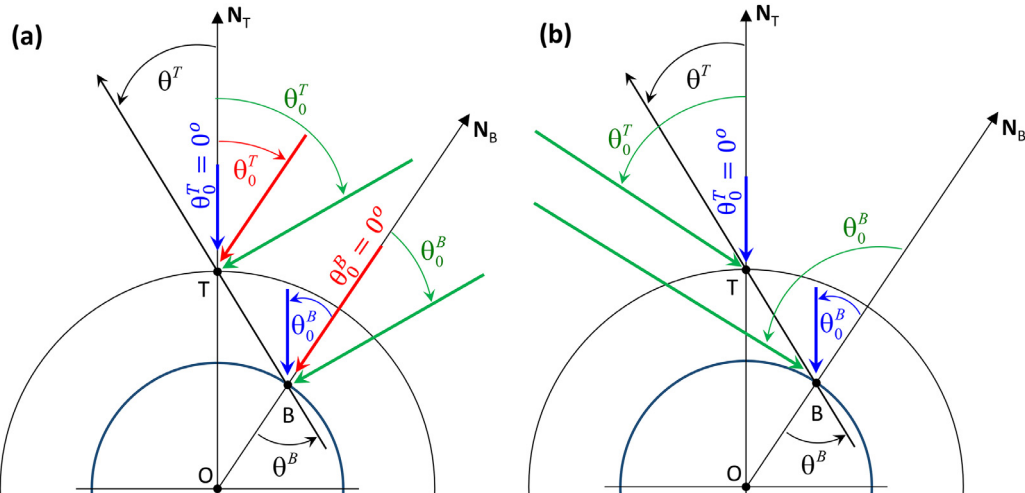


Fig. 4. (a): Different solar-view geometries in the principal plane 0° – 180° . The outgoing view direction (black) is given, the solar direction varies (green, red - critical, blue). This image corresponds to $\varphi_{TOA} = 0^\circ$. (b): Same as Fig. 4(a), except for $\varphi_{TOA} = 180^\circ$. There is no critical (red) solar beam direction in this case.

$\theta_{0,TOA}^{Critical}, \varphi_{BOA} = 180^\circ, \theta_{0,TOA} + \theta_{TOA} = \theta_{BOA} - \theta_{0,BOA}$ - note the minus sign.

$\theta_{0,TOA} = 0^\circ$ falls under the “blue” case; also, this is the smallest possible $\theta_{0,TOA} = 0^\circ$ defines the largest possible $\theta_{0,BOA}$ (in the $\varphi_{BOA} = 180^\circ$ half-plane) for any given VZA on TOA.

Case 2: $\varphi_{TOA} = 180^\circ$, Fig. 4(b).

In this case, $\varphi_{BOA} = 180^\circ$ for any sun position. The BOA SZA is computed as

$$\theta_{0,BOA} = \theta_{0,TOA} + \theta_{BOA} - \theta_{TOA}.$$

However, there is a critical SZA at TOA for which the observed point is no longer irradiated by the Sun:

$$\theta_{0,BOA} = 90 = \theta_{0,TOA} + \theta_{BOA} - \theta_{TOA} \Rightarrow \theta_{0,TOA} = 90 + \theta_{TOA} - \theta_{0,TOA}.$$

The solar-view geometry at TOA and BOA used to reproduce the A & K results is listed in Table 1, with 2 significant digits after the decimal point. Appendix 3 below discusses the case of the Earth shadow.

Appendix 2: General Transformation of the Solar-View Geometry from BOA to TOA and vice versa

From Eq. (2) and the procedure outlined in Appendix 1, we see that some solar-view geometries at TOA have no corresponding configurations at BOA, thanks to the line of sight not hitting hit the Earth and/or the point of observation is in the Earth shadow (see Appendix 3). Therefore, in atmospheric and terrestrial applications, the solar-view geometry is often defined at BOA. In this Appendix 2 we provide equations to transform the solar-view geometry from BOA to TOA for arbitrary relative azimuth. After that, we “invert” the problem in order to compute input for VLIDORT (BOA) from the given TOA angles (input for A & K and MYSTIC). Fig. 5 shows the geometry.

From Eq. (2), one readily computes $\theta_B \geq \theta_T$. Further the angle, α , between the two local normal vectors at TOA and BOA is

$$\alpha = \theta_B - \theta_T. \quad (9)$$

The coordinates of the TOA local normal in the earth-centered coordinate system are

$$\mathbf{n}_T = [\sin \alpha \cos \varphi_B \quad \sin \alpha \sin \varphi_B \quad \cos \alpha] \quad (10)$$

and the solar beam direction is

$$\mathbf{l}_0 = [\sin \theta_{0,B} \quad 0 \quad -\cos \theta_{0,B}] \quad (11)$$

with respect to the BOA normal pointing towards the space (hence, $z_0 = -\cos \theta_{0,B} \leq 0$). The cosine of the solar angle at TOA comes

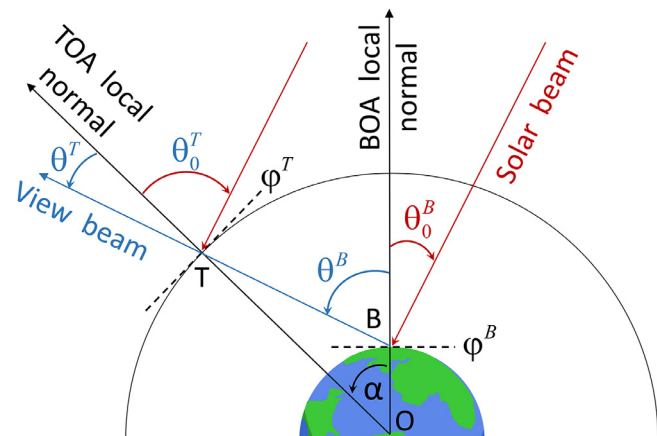


Fig. 5. The solar-view geometry, and TOA and BOA local normal vectors. Note, the scattering angle is the same at arbitrary point in atmosphere.

from the dot product of Eqs. (10) and (11)

$$\cos(180 - \theta_{0,T}) = \mathbf{l}_0 \mathbf{n}_T = \sin \alpha \sin \theta_{0,B} \cos \varphi_B - \cos \alpha \cos \theta_{0,B} = -\cos \theta_{0,T} \quad (12)$$

Equality of the scattering angle, Θ , at TOA and BOA yields the TOA azimuth

$$\cos \Theta = -\cos \theta_B \cos \theta_{0,B} + \sin \theta_B \sin \theta_{0,B} \cos \varphi_B = -\cos \theta_T \cos \theta_{0,T} + \sin \theta_T \sin \theta_{0,T} \cos \varphi_T. \quad (13)$$

except for the case of normal irradiance of the TOA, $\cos \theta_{0,T} = 0^\circ$ in Eq. (12), when the azimuth at BOA is undefined, and also for the exact nadir observation situation, $\sin \theta_T = \sin \theta_B = 0^\circ$.

There is an inevitable loss of accuracy due to multiple use of trigonometric functions. This results in $\varphi_T \neq 0^\circ$ or $\varphi_T \neq 180^\circ$ in the principal plane. If critical, the developer should consider the case of the observation in the principal plane separately (Appendix 1) or if-check φ_T to be “sufficiently close” to 0° or 180° .

If on the other hand the BOA geometry is to be computed from the TOA configuration, then one looks for $\theta_{0,B}$ and φ_B (recall, θ_B comes from Eq. (1)) from this system of Eqs. (12)–(13)

$$\begin{cases} \sin \alpha \sin \theta_{0,B} \cos \varphi_B - \cos \alpha \cos \theta_{0,B} = -\cos \theta_{0,T} \\ \sin \theta_B \sin \theta_{0,B} \cos \varphi_B - \cos \theta_B \cos \theta_{0,B} = \cos \Theta \end{cases}, \quad (14)$$

or in matrix form

$$\begin{bmatrix} -\sin \alpha & \cos \alpha \\ \sin \theta_B & -\cos \theta_B \end{bmatrix} \begin{bmatrix} \sin \theta_{0,B} \cos \varphi_B \\ \cos \theta_{0,B} \end{bmatrix} = \begin{bmatrix} -\cos \theta_{0,T} \\ \cos \Theta \end{bmatrix}, \quad (15)$$

where singular matrix cases (e.g. for exact nadir observation) must be treated separately.

Appendix 3: Azimuthal Location of Points in the Earth Shadow

In this Appendix we derive equations to find the TOA azimuths that correspond to sunlit points at the surface level. Figs. 6(a) and (b), for pure Rayleigh scattering and scattering with some aerosol loading, respectively, show “sudden” drops of intensity when plotted against the TOA azimuth. This effect is captured by a true-spherical code such as MYSTIC. Fig. 6(c) explains the effect: points A and B are always visible, while points E, D, and C disappear into the Earth shadow in that order when the LOS rotates from the forward scattering, $\varphi_{TOA} = 0^\circ$, to the backscattering, $\varphi_{TOA} = 180^\circ$, geometry.

From the right-angle triangle PEO, $PE^2 = R_E^2 - OE^2$; from the right-angle triangle SEO, $OE = SO \sin(\alpha)$; and the distance to the point of observation is

$$SP = SE - PE = SO \cos(\alpha) - \sqrt{R_E^2 - SO^2 \sin^2(\alpha)}$$

Using Heron's rule for the area of SPO

$$\Delta_{SPO} = \sqrt{p(p - R_E)(p - SO)(p - SP)},$$

where p is the semi-perimeter of SPO, we can derive the height of the SPO triangle:

$$PA = 2\Delta_{SPO}/SO.$$

From the triangles PAO and TAO we find that $AO = \sqrt{R_E^2 - PA^2}$ and $TA = AO/\tan(\theta_0)$, respectively. If $TA < PA$, the range of visible azimuths is defined from the right image of Fig. 7 as

$$\varphi_{\max} = 180^\circ - \phi = 180^\circ - \arccos(TA/PA).$$

Otherwise, all azimuths are visible from S and the given solar-view geometry. This includes the particular case of $\theta_0 \rightarrow 0^\circ$.

Fig. 7 shows the range of sunlit azimuths as $180^\circ - \phi$, where ϕ values correspond to the TOA azimuths of those points in the Earth shadow. We suppose the satellite S, is located at a height SB above the ground and P is a point on the ground surface observed at scan angle α . The solar beam direction and the satellite nadir span an angle θ_0 .

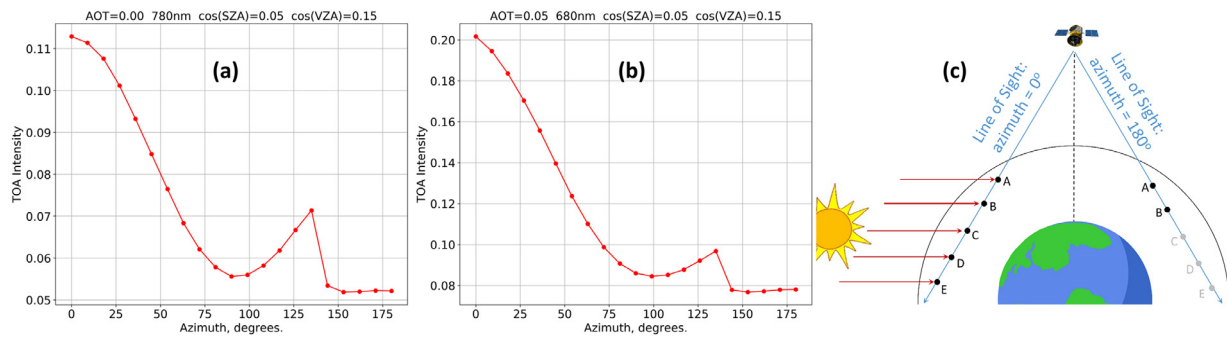


Fig. 6. Reflected intensity (y-axis) as a function of the TOA azimuth (x-axis) and AOT (image (a) vs (b)). The Earth shadow causes drops near 135° azimuth: points A & B are visible for any azimuth, while C, D, and E “disappear” into the Earth shadow in the backscattering directions as shown in image (c).

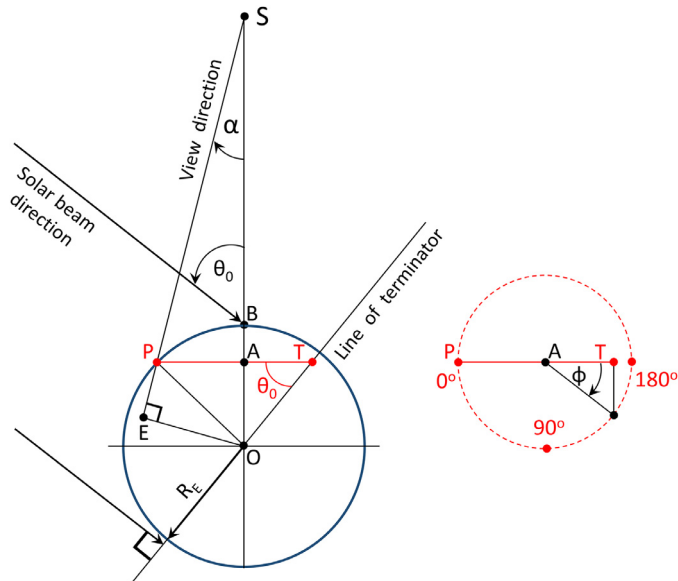


Fig. 7. Geometrical sketch to define the range of the “sunlit azimuths”; R_E is the Earth radius.

References

- [1] Adams CN, Kattawar GW. Radiative transfer in spherical shell atmospheres. I. Rayleigh scattering. *Icarus* 1978;35:139–51.
- [2] Yu Belikov, Yu Romanovsky, Sh Nikolashvili, Paradze R. Numerical model of scattering radiation in the Earth atmosphere for scientific investigations and applications. *Phys. Chem. Earth (B)* 2000;25(5–6):427–30.
- [3] Bellman R, Kagiwada H, Kalaba R. Invariant imbedding and radiative transfer in spherical shells. *J. Comp. Phys.* 1967;2:245–56.
- [4] Bellman R, Kagiwada H, Kalaba R, Ueno S. Diffuse reflection of solar rays by a spherical shell atmosphere. *Icarus* 1969;11:417–23.
- [5] Blättner WG, Horak HG, Collins DG, Wells MB. Monte Carlo studies of the sky radiance at twilight. *Appl Opt* 1974;13(3):534–46.
- [6] Bourassa AE, Degenstein DA, Llewellyn EJ. SASKTRAN: a spherical geometry radiative transfer code for efficient estimation of limb scattering sunlight. *J. Quant. Spectrosc. Radiat. Transfer* 2008;109:52–73.
- [7] Buehler SA, Mendrok J, Eriksson P, Perrin A, Larsson R, Lemke O. ARTS, the atmospheric radiative transfer simulator — Version 2.2, the planetary toolbox edition. *Geosci. Model Dev.* 2018;11(4):1537–56.
- [8] Buras R, Mayer B. Efficient unbiased variance reduction techniques for Monte Carlo simulations of radiative transfer in cloudy atmospheres: the solution. *J. Quant. Spectrosc. Radiat. Transfer* 2011;112:434–47.
- [9] Caudill TR, Flittner DE, Herman BM, Torres O, McPeters RD. Evaluation of the pseudo-spherical approximation for backscattered ultraviolet radiances and ozone retrieval. *J. Geophys. Res* 1997;102(D3):3881–90.
- [10] Chowdhary J, Zhai P-W, Xu F, Frouin R, Ramon D. Testbed results for scalar and vector radiative transfer computations of light in atmosphere-ocean systems. *J. Quant. Spectrosc. Radiat. Transfer* 2020;242:106717.
- [11] Collins DG, Blättner WG, Wells MB, Horak HG. Backward Monte Carlo calculations of the Polarization characteristics of the radiation emerging from spherical-shell atmospheres. *Appl Opt* 1972;11(11):2684–96.
- [12] Dahlback A, Stamnes K. A new spherical model for computing the radiation field available for photolysis and heating at twilight. *Planet Space Sci* 1991;39(5):671–83.
- [13] Davis C, Emde C, Harwood R. A 3-D polarized reversed Monte Carlo radiative transfer model for millimeter and submillimeter passive remote sensing in cloudy atmospheres. *IEEE Trans. Geosci. Rem. Sens* 2005;43(5):1096–101.
- [14] Davison B. Neutron transport theory. Oxford University Press; 1958.
- [15] Ding K, Gordon HR. Atmospheric correction of ocean-color sensors: effects of the Earth’s curvature. *Appl. Opt* 1994;33(30):7096–106.
- [16] Doicu A, Trautmann T. Discrete-ordinate method with matrix exponential for a pseudospherical atmosphere: scalar case. *J. Quant. Spectrosc. Radiat. Transfer* 2009;110:146–58.
- [17] Doicu A, Trautmann T. Discrete-ordinate method with matrix exponential for a pseudospherical atmosphere: vector case. *J. Quant. Spectrosc. Radiat. Transfer* 2009;110:159–72.
- [18] Doicu A, Trautmann T. Adjoint problem of radiative transfer for a pseudo-spherical atmosphere and general viewing geometries. *J. Quant. Spectrosc. Radiat. Transfer* 2009;110:464–76.
- [19] Doicu A, Trautmann T. Picard iteration methods for a spherical atmosphere. *J. Quant. Spectrosc. Radiat. Transfer* 2009;110:1851–63.
- [20] Dubovik O, et al. Polarimetric remote sensing of atmospheric aerosols: instruments, methodologies, results, and perspectives. *J. Quant. Spectrosc. Radiat. Transfer* 2019;224:474–511.
- [21] Dueck SRF, Bourassa AE, Degenstein D. An efficient algorithm for polarization in the SASKTRAN radiative transfer framework. *J. Quant. Spectrosc. Radiat. Transfer* 2017;199:1–11.
- [22] Efremenko DS, Doicu A, Loyola D, Trautmann T. Small-angle modification of the radiative transfer equation for a pseudo-spherical atmosphere. *J. Quant. Spectrosc. Radiat. Trans.* 2013;114:82–90.
- [23] Eluszkiewicz J, Uymin G, Flittner D, Cady-Pereira K, Malwer E, Henderson J, Moncet J-L, Nehrkorn T, Wolff M. A fast code for channel limb radiances with gas absorption and scattering in a spherical atmosphere. *J. Quant. Spectrosc. Radiat. Trans.* 2017;193:31–9.
- [24] Emde C, Buehler SA, Davis C, Eriksson P, Sreerekha TR, Teichmann C. A polarized discrete ordinate scattering model for simulations of limb and nadir long-wave measurements in 1-D/3-D spherical atmosphere. *J. Geophys. Res.* 2004;109:D24207.
- [25] Emde C, Mayer B. Simulation of solar radiation during a total solar eclipse: a challenge for radiative transfer. *Atmos. Chem. Phys.* 2007;7:2259–70.
- [26] Emde C, Barlakas V, Cornet C, Evans F, Korkin S, Ota Y, Labonnote LC, Lyapustin A, Macke A, Mayer B, Wendisch M. IPRT polarized radiative transfer model intercomparison project – Phase A. *J. Quant. Spectrosc. Radiat. Trans.* 2015;164:8–36.
- [27] Emde C, Buras-Schnell R, Kylling A, Mayer B, Gasteiger J, Hamann U, Kylling J, Richter B, Pause C, Dowling T, Bugliaro L. The libRadtran software package for radiative transfer calculations (version 2.0.1). *Geoscientific Model Dev.* 2016;9(5):1647–72.
- [28] Emde C, Buras R, Sterzik M, Bagnulo S. Influence of aerosols, clouds, and sunglint on polarization spectra of Earthshine. *Astron. Astrophys* 2017;605(A2).
- [29] Eriksson P, Buehler SA, Davis CP, Emde C, Lemke O. ARTS, the atmospheric radiative transfer simulator, version 2. *J. Quant. Spectrosc. Radiat. Trans.* 2011;112:1551–8.
- [30] Garcia RDM, Siewert C. A numerically stable spherical harmonics solution for the neutron transport equation in a spherical shell. *J. Quant. Spectrosc. Radiat. Trans.* 2020;405:109139.
- [31] Gratia SL, Levin DA, Walker AC. Rassvet: backward Monte Carlo radiative transfer in spherical-shell planetary atmospheres. *Icarus* 2010;206:366–79.
- [32] Gratia SL, Walker AC, Levin DA, Goldstein DB, Varghese PL, Trafton LM, et al. Multi-wavelength simulations of atmospheric radiation from Io with a 3-D spherical-shell backward Monte Carlo radiative transfer model. *Icarus* 2010;207:394–408.
- [33] Griffioen E, Oikarinen L. LIMBTRAN: a pseudo three dimensional radiative transfer model for the limb-viewing imager OSIRIS on the ODIN satellite. *J. Geophys. Res.* 2000;105:29717–30 2000.

- [34] Herman BM, Ben-David A, Thome JK. Numerical technique for solving the radiative transfer equation for spherical shell atmosphere. *Appl. Opt.* 1994;33(9):1760–70.
- [35] Herman BM, Caudill T, Flittner D, Liou K-N. Comments on “Solar heating rates: the importance of spherical geometry”. *J. Atmos. Sci.* 1995;52(3):380–2.
- [36] Herman BM, Caudill TR, Flittner DE, Thome KJ, Ben-David A. Comparison of the Gauss-Seidel spherical polarized radiative transfer code with other radiative transfer codes. *Appl. Opt.* 1995;34(21):4563–72.
- [37] He X, Stamnes K, Bai Y, Li W, Wang D. Effects of Earth curvature on atmospheric correction for ocean color remote sensing. *Remote Sens Environ.* 2018;209:118–33.
- [38] Holben BN, Eck TF, Slutsker I, Tanré D, Buis JP, Setzer A, Vermote E, Reagan JA, Kaufman YJ, Nakajima T, Lavenue F, Jankowiak I, Smirnov A. AERONET-A federated instrument network and data archive for aerosol characterization. *Rem. Sens. Env.* 1998;66:1–16.
- [39] Ž Ivezić, MAT Groenwegen, Men'shchikov A, Szczerba R. Benchmark problems for dust radiative transfer. *Mon. Not. R. Astron. Soc.* 1997;291:121–4.
- [40] Kalkofen W, editor. *Methods in radiative transfer*. Cambridge University Press; 1984.
- [41] Kattawar GW, Adams CN. Radiative transfer in spherical shell atmospheres. II. Asymmetric phase function. *Icarus* 1978;35:436–49.
- [42] Kattawar GW. Radiative transfer in spherical shell atmosphere. III. Application to Venus. *Icarus* 1979;40:60–6.
- [43] Kocifaj M. Multiple scattering contribution to the diffuse light of a night sky: a model which embraces all orders of scattering. *J. Quant. Spectrosc. Rad. Trans.* 2018;206:260–72.
- [44] Korkin S, Lyapustin A, Sinyuk A, Holben B, Kokhanovsky A. Vector radiative transfer code SORD: performance analysis and quick start guide. *J. Quant. Spectrosc. Rad. Trans.* 2017;200:295–310.
- [45] Korkin S, Lyapustin A. Matrix exponential in C/C++ version of vector radiative transfer code IPOL. *J. Quant. Spectrosc. Rad. Trans.* 2019;227:106–10.
- [46] Kylling A, Stamnes K, Tsay S-C. A reliable and efficient two-stream algorithm for spherical radiative transfer: documentation of accuracy in realistic layered media. *J. Atmos. Chem.* 1995;21:115–50.
- [47] Laszlo I, Stamnes K, Wiscombe W, Tsay S-C. The discrete ordinate algorithm, DISORT for radiative transfer. In: Kokhanovsky A, editor. *Light scattering reviews 11*; 2017. p. 3–65. Springer.
- [48] Lenoble J, Sekera Z. Equation of radiative transfer in a planetary spherical atmosphere. *Proc. Nat. Acad. Sci. USA* 1961;47:372–8.
- [49] Lenoble J, editor. *Radiative transfer in scattering and absorbing atmospheres: standard computational procedures*. Hampton VA: A. Deepak Publishing; 1985.
- [50] Lenoble J. *Atmospheric radiative transfer*. Hampton VA: A. Deepak Publishing; 1993.
- [51] Loughman RP, Griffioen E, Oikarinen L, Postlyakov OV, Rozanov A, Flittner DE, Rault DF. Comparison of radiative transfer sunlight measurements. *J. Geograph. Res.* 2004;109:D06303.
- [52] Loughman R, Flittner D, Nyaku E, Bhartia PK. Gauss-Seidel limb scattering (GSL) radiative transfer model development in support of the Ozone Mapping and Profiler Suite (OMPS) limb profiler mission. *Atmos. Chem. Phys* 2015;15:3007–20.
- [53] Lyapustin A, Wang Y, Korkin S, Huang D. MODIS collection 6 MAIAC algorithm. *Atmos. Meas. Tech.* 2018;11:5741–65.
- [54] Marchuk GI, Mikhailov GA, Nazarov MN, Darbinjan RA, Kargin BA, Elepov BS. The monte carlo method in atmospheric optics. Berlin: Springer; 1980.
- [55] Mayer B, Seckmeyer G, Kylling A. Systematic long-term comparison of spectral UV measurements and UVSPEC modeling results. *J. Geophys. Res.* 1997;102:8755–67.
- [56] Mayer B, Kylling A. Technical note: the libRadtran software package for radiative transfer calculations - description and examples of use. *Atmos. Chem. Phys* 2005;5:1855–77.
- [57] Mayer B. Radiative transfer in the cloudy atmosphere. *Eur. Phys. J. Conf.* 2009;1:75–99.
- [58] McCartney EJ. *Optics of the atmosphere. scattering by molecules and particles*. New York NY: John Wiley & Sons; 1976.
- [59] McLinden CA, McConnell JC, Griffioen E, McElroy CT. A vector radiative-transfer model for the Odin/OSIRIS project. *Can. J. Phys* 2002;80:375–93.
- [60] Nataraj V, Spurr RJD. A fast linearized pseudo-spherical two orders of scattering model to account for polarization in vertically inhomogeneous scattering-absorbing media. *J. Quant. Spectrosc. Rad. Trans.* 2007;107:263–93.
- [61] Natsuyama HH, Ueno S, Wang AP. *Terrestrial radiative transfer. modeling, computation, and data analysis*. Springer; 1998.
- [62] Oikarinen L, Sihvola E, Kyrölä E. Multiple scattering radiance in limb-viewing geometry. *J. Geophys. Res.* 1999;104(D24):31261–74.
- [63] Ockenfuß P, Emde C, Mayer B, Bernhard G. Accurate 3D radiative transfer simulation of spectral solar irradiance during the total solar eclipse of August 21, 2017. *Atmos. Chem. Phys. Discuss* 2019:609.
- [64] Petropavlovskikh I, Loughman R, DeLuise J, Herman B. A comparison of UV intensities calculated by spherical atmosphere radiation transfer codes: application to aerosol corrections. *J. Geophys. Res.* 2000;105(D11):14737–46.
- [65] Postlyakov OV, Oikarinen L, Kyrölä W. Fine comparison of radiative transfer models for scattering limb simulation. *Geophys. Res. Abs* 2003;5:05566.
- [66] Postlyakov OV. Linearized vector radiative transfer model MCC++ for a spherical atmosphere. *J. Quant. Spectrosc. Rad. Trans.* 2004;88:297–317.
- [67] Postlyakov OV. Radiative transfer model MCC++ with evaluation of weighting functions in spherical atmosphere for use in retrieval algorithms. *J. Quant. Spectrosc. Rad. Trans.* 2004;34:721–6.
- [68] Premuda M, Palazzi E, Ravegnani F, Bortoli D, Masieri S, Giovanelli G. MOCRA: a Monte Carlo code for the simulation of radiative transfer in the atmosphere. *Opt Express* 2012;20(7):7973–93.
- [69] Ramon D, Steinmetz F, Jolivet D, Compiegne M, Frouin R. Modelling polarized radiative transfer in the ocean-atmosphere system with the GPU-accelerated SMART-G Monte Carlo code. *J. Quant. Spectrosc. Rad. Trans.* 2019;222–223:89–107.
- [70] Rozanov AV, Rozanov VV, Burrows JP. Combined differential-integral approach for the radiation field computation in spherical shell atmosphere: nonlimb geometry. *J. Geophys. Res.* 2000;105(D18):22937–42.
- [71] Rozanov A, Rozanov V, Burrows JP. A numerical radiative transfer model for a spherical planetary atmosphere: combined differential-integral approach involving the Picard iterative approximation. *J. Quant. Spectrosc. Rad. Trans.* 2001;69:491–512.
- [72] Rozanov A, Rozanov V, Burrows JP. Evaluation of the combined differential-integral approach for limb viewing geometry. *Adv. Space Res* 2002;29(11):1843–8.
- [73] Rozanov VV, Buchwitz M, Eichmann K-U, de Beek R, Burrows JP. SCIATRAN - a new radiative transfer model for geophysical applications in the 240–2400 nm spectral region: the pseudo-spherical version. *Adv. Space. Res* 2002;29:1831–5.
- [74] Rozanov A, Rozanov V, Buchwitz M, Kokhanovsky A, Burrows JP. SCIATRAN - a new radiative transfer model for geophysical applications in the 240–2400 nm spectral region. *Adv. Space Res* 2005;36:1015–19.
- [75] Rozanov V, Rozanov A, Kokhanovsky A, Burrows J. Radiative transfer through terrestrial atmosphere and ocean: software package SCIATRAN. *J. Quant. Spect. Rad. Trans.* 2014;133:13–71.
- [76] Rozenberg GV. *Twilight. a study in atmospheric optics*. Springer Science + Business Media; 1966.
- [77] Sen KK, Wilson SJ. *Radiative transfer in curved media*. Singapore: World Scientific; 1990.
- [78] Sinyuk A, Holben BN, Eck TF, Giles DM, Slutsker I, Korkin S, Schafer JS, Smirnov A, Sorokin M, Lyapustin A. The AERONET Version 3 aerosol retrieval algorithm, associated uncertainties and comparisons to Version 2. *Atmos. Meas. Tech. Discuss* 2020:474.
- [79] Smokty OI. Multiple light scattering in the spherical planetary atmosphere. *Pure Appl. Geophys* 1969;72:214–26.
- [80] Sobolev VV. *Light scattering in planetary atmospheres*. Oxford: Pergamon Press; 1975.
- [81] Spada F, Krol MC, Stamnes P. McSCIA: application of the Equivalence Theorem in a Monte Carlo radiative transfer model for spherical shell atmospheres. *Atmos. Chem. Phys* 2006;6:4823–42.
- [82] Spurr RJD. Simultaneous derivation of intensities and weighting functions in a general pseudo-spherical discrete ordinate radiative transfer treatment. *J. Quant. Spectrosc. Rad. Trans.* 2002;75:129–75.
- [83] Spurr RJD. LIDORT V2PLUS: a comprehensive radiative transfer package for UV/VIS/NIR nadir remote sensing. *Proc. SPIE* 2004;5235:89–100.
- [84] Spurr R, Christi M. The LIDORT and VLIDORT linearized scalar and vector discrete ordinate radiative transfer models: updates in the last 10 years. Springer series in light scattering. Kokhanovsky A, editor; 2019.
- [85] Stamnes K, Tsay SC, Wiscombe W, Jayaweera K. Numerically stable algorithm for discrete-ordinate-method radiative transfer in multiple scattering and emitting layered media. *Appl Opt* 1988;27(12):2502–9.
- [86] Stamnes K, Thomas GE, Stamnes J. *Radiative transfer in the atmosphere and ocean*. 2nd edition. Cambridge: Cambridge University Press; 2017.
- [87] Truitt Wiensz J, Bourassa AE, Lloyd ND, Wiacek A, Martin RV, Degenstein DA. Photon conservation in scattering by large ice crystals with the SASKTRAN radiative transfer model. *J. Quant. Spectrosc. Rad. Trans.* 2012;113:582–93.
- [88] Tzortziou M, Krotkov N, Cede A, Herman JR, Vasilkov A. A new technique for retrieval of tropospheric and stratospheric ozone profiles using sky radiance measurements at multiple view angles: application to a Brewer spectrometer. *J. Geophys. Res.* 2008;113:D06304.
- [89] Unno W, Kondo M. The Eddington approximation generalized for radiative transfer in spherically symmetric systems. I. Basic method. *Publ. Astron. Soc. Japan* 1976;28:347–54.
- [90] van Oss RF, Spurr RJD. Fast and accurate 4 and 6 stream linearized discrete ordinate radiative transfer models for ozone profile retrieval. *J. Quant. Spectrosc. Rad. Trans.* 2002;75:177–220.
- [91] Walter HH, Landgraf J, Hasekamp OP. Linearization of pseudo-spherical vector radiative transfer model. *J. Quant. Spectrosc. Rad. Trans.* 2004;85:251–83.
- [92] Walter HH, Landgraf J. Towards linearization of atmospheric radiative transfer in spherical geometry. *J. Quant. Spectrosc. Rad. Trans.* 2005;95:175–200.
- [93] Walter HH, Landgraf J, Spada F, Doicu A. Linearization of a radiative transfer model in spherical geometry. *J. Geophys. Res.* 2006;111 D24304.
- [94] Wilson SJ, Sen KK. Light scattering by an optically thin inhomogeneous, spherically-symmetric planetary atmosphere: brightness at the zenith near the terminator. *Astrophysics and Space Science* 1980;71:405–10.
- [95] Xu F, West RA, Davis AB. A hybrid method for modelling polarized radiative transfer in a spherical-shell planetary atmosphere. *J. Quant. Spectrosc. Rad. Trans.* *J. Quant. Spectrosc. Rad. Trans.* 2013;117:59–70.
- [96] Zawada DJ, Dueck SR, Rieger LA, Bourassa AE, Lloyd ND, Degenstein DA. High-resolution and Monte Carlo additions to the SASKTRAN radiative transfer model. *Atmos. Meas. Tech* 2015;8:2609–23.
- [97] Zhuravleva T, Nasrtdinov I, Chesnokova T, Ptashnik I. Monte Carlo simulation of thermal radiative transfer in spatially inhomogeneous clouds taking into account the atmospheric sphericity. *J. Quant. Spectrosc. Rad. Trans.* 2019;236:106602.